JACS
JOURNAL OF THE AMERICAN CHEMICAL SOCIETY
Article
pubs.acs.org/JACS

Dipole-Mediated Rectification of Intramolecular Photoinduced Charge Separation and Charge Recombination

Duoduo Bao,[†,⊥] Srigokul Upadhyayula,[†,‡,#] Jillian M. Larsen,[†] Bing Xia,[†,▽] Boriana Georgieva,[†] Vicente Nuñez,[†] Eli M. Espinoza,[§] Joshua D. Hartman,[§] Michelle Wurch,[†] Andy Chang,[†] Chung-Kuang Lin,[†] Jason Larkin,[†] Krystal Vasquez,[§] Gregory J. O. Beran,*[,§] and Valentine I. Vullev*[,†,‡,§,∥]

[†]Department of Bioengineering, [‡]Department of Biochemistry, [§]Department of Chemistry, and [∥]Materials Science and Engineering Program, University of California, Riverside, California 92521, United States

Supporting Information

ABSTRACT: Controlling charge transfer at a molecular scale is critical for efficient light harvesting, energy conversion, and nanoelectronics. Dipole-polarization electrets, the electrostatic analogue of magnets, provide a means for "steering" electron transduction via the local electric fields generated by their permanent electric dipoles. Here, we describe the first demonstration of the utility of anthranilamides, moieties with ordered dipoles, for controlling intramolecular charge transfer. Donor–acceptor dyads, each containing a single anthranilamide moiety, distinctly rectify both the forward photoinduced electron transfer and the subsequent charge recombination. Changes in the observed charge-transfer kinetics as a function of media polarity were consistent with the anticipated effects of the anthranilamide molecular dipoles on the rectification. The regioselectivity of electron transfer and the molecular dynamics of the dyads further modulated the observed kinetics, particularly for charge recombination. These findings reveal the underlying complexity of dipole-induced effects on electron transfer and demonstrate unexplored paradigms for molecular rectifiers.

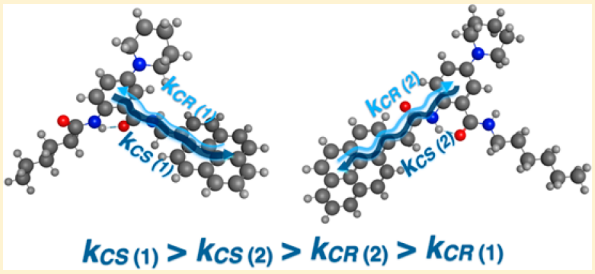

INTRODUCTION

At a molecular level, *charge-transfer rectification* is a term borrowed from electrical engineering to represent preferred directionality of electron entrainment.[1] Molecular rectifiers are some of the principal building blocks for nanoscale electronics.[2−4] Accelerating forward charge transfer (CT) and impeding charge recombination (CR) via charge-transfer rectification are particularly important for energy-conversion applications.[5]

In the context of electrical engineering and molecular electronics, rectification is defined in terms of charge transport, i.e., how the magnitude of the electric current depends on the direction of the applied potential. However, numerous device features, such as the interfaces with the molecules, can dominate charge-transport rectification.[6,7] Therefore, charge-transfer rectification, representing the dependence of the CT rates on the direction of intramolecular electron transfer, allows for unequivocal examination of molecular features that govern these processes.

Rectification behavior results from asymmetry in CT pathways. Local electric fields generated by molecular electric dipoles provide a means for attaining such asymmetry. Therefore, conjugates with codirectionally ordered electric dipoles represent an important class of molecular rectifiers.

Similar to a molecular magnet,[8,9] a *molecular electret* is a conjugate containing polar groups with a codirectional arrangement of their permanent electric dipole moments.[10,11] With large intrinsic dipoles oriented along their axes, protein helices are some of the best-known molecular electrets.[12−15] Ordered amides and hydrogen-bonding networks in protein α-helices and 3_{10}-helices produce intrinsic electric dipoles of about five Debyes per residue.[16−18] Polyproline helices, which lack hydrogen bonding along their backbones, have intrinsic dipoles that are smaller or oppositely oriented in comparison with α-helices.[18] These dipoles, oriented along the helix axis, can rectify electron transfer[19−27] and aid ion transport.[12−14]

Galoppini and Fox were first to report the dipole-induced rectification of long-range CT using helices with a donor and an acceptor attached to them.[19,20,28] The electron transfer (ET) toward the positive pole of the helix dipole was faster than the ET toward the negative pole.[19,20,28]

Since these first reports,[19,20,28] dipole effects on CT have been studied almost exclusively in helical polypeptides.[21−27,29] Self-assembled monolayers of polypeptide helices on gold exhibited rectification consistent with the orientation of their dipoles.[21,22,26] A recent report on proline peptides with three different redox residues showed that charges have a similar effect on CT.[23] Electrical junctions, comprising layers of zwitterionic conjugates or of polypeptide α-helices, manifested a pronounced dipole-induced current rectification.[30−33]

Received: June 9, 2014
Published: August 27, 2014

dx.doi.org/10.1021/ja505618n | J. Am. Chem. Soc. 2014, 136, 12966−12973

The electrets are dielectrics, which presents a fundamental challenge in using them as charge-transfer media. Protein helices are no exception: their large HOMO−LUMO gaps and inaccessible reduction potentials render these biomolecular electrets largely ineffectual for electronic applications (HOMO = highest occupied molecular orbital, and LUMO = lowest unoccupied molecular orbital). The peptide bonds, which are aliphatic amides, have the narrowest HOMO−LUMO gaps (exceeding 5 eV) along the protein backbones, and they are not good electron donors or acceptors. Unless the CT pathways involve redox residues or cofactors with sufficient electronic coupling between them,[34] proteins mediate ET via a superexchange mechanism, i.e., tunneling along virtual states, limiting its efficiency to about 2 nm.[35−37] The irreversible electrochemical oxidation of aliphatic amides has peak potentials between 1.3 and 1.8 V versus SCE and leads to bond cleavage.[38] Hence, to prevent decomposition of these biopolymers, the peptide bonds cannot be durable sites for charges (holes, in particular), and tunneling accounts for the experimentally observed features of CT through polypeptides.[18,44]

We have undertaken a bioinspired approach[45] in designing molecular electrets that possess the electronic advantages of protein helices, that is, ordered amide and hydrogen bonds that generate intrinsic dipoles of about 3 to 5 D per residue (Chart 1a).[10,11,45] Unlike their biological counterparts, the bioinspired electrets based on anthranilamides are composed of covalently linked aromatic moieties, forming extended π-conjugation along their backbones (Chart 1a). Such a sequence of electronically coupled aromatic residues is essential for attaining long-range charge transfer via electron- or hole-hopping mechanisms. Furthermore, altering the substituents on the aromatic residues of the synthetic electrets (R_1 and R_2 in Chart 1a) allows for adjusting their electronic properties, enabling efficient long-range electron or hole entrainment.[11]

Chart 1. Bioinspired Electrets Based on Anthranilamides[a]

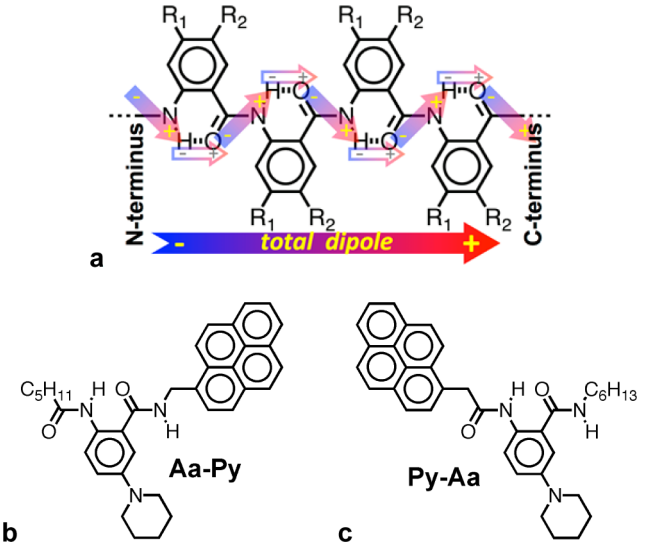

[a](a) Intrinsic electric dipole moment of anthranilamide electrets originates from (1) the ordered orientation of the amide-bond dipoles (solid arrows); and (2) the change in the polarization due to the shift in the electron density from O to H upon hydrogen-bond formation (hollow arrows). Unlike protein α-helices, the anthranilamide dipole is oriented from the N- to the C-terminus. (b, c) Donor−acceptor dyads with the acceptor linked to (b) the C-terminus and (c) the N-terminus of the anthranilamide residue.

In order for the anthranilamides to have utility as charge-transfer electrets, they have to (1) rectify CT; (2) have wide HOMO−LUMO gaps, typical for dielectrics; (3) possess no permanent charges; and (4) accommodate charges on their residues without initiating undesired decomposition processes. That is, the residues have to manifest reversible oxidation or reduction. The second requirement is important for preventing the thermal generation of free charge carriers and semiconducting type electronic characteristics. Such mobile free charges can readily redistribute and screen the local fields, thus suppressing the dipole effects. Similar to polar solvents, free counterions in the surrounding media can have the same screening effect, implementing the reason for the third requirement. While this requirement is not truly strict, it can be viewed as a recommendation for preventing additional complexity in the interpretation of the field effects on charge transfer. Finally, the fourth requirement is especially important for attaining long-range electron or hole hopping.

As a first step toward development of charge-transfer molecular electrets, we focus here on a single anthranilamide residue, 2-alkanamido-*N*-alkyl-5-(piperidin-*N*-yl)benzamide, Aa (see Supporting Information). Aa exhibits reversible electrochemical oxidation. Its zero-to-zero energy, E_{00}, is about 3 eV, and its permanent dipole moment is about 6 D. Hence, this residue is potentially a promising building block of an electret dielectric that can mediate hole hopping. Most importantly, we demonstrate here the Aa moiety rectifies the directionality of forward and back electron transfer to and from a covalently linked acceptor (Chart 1b,c). While most previous reports have focused on the dipole effects on charge separation (CS),[18−21] and a few have discussed charge recombination (CR),[46] here we examine the rectification of both, the forward and back CT.

For the initial photoinduced CS, the rates of ET along the Aa dipole are up to 6.4 times faster than the ET rates against the dipole. This degree of rectification is particularly impressive for a single residue. For comparison, reported rates of ET along and against the dipole in a polypeptide helix with 14 residues differ 27-fold for optimal conditions, i.e., for a relatively nonpolar media.[19,20] The dependence on the media polarity suggests that the Aa dipole governs the observed CT rectification. The picosecond CS kinetics is further modulated by molecular dynamics, while ET regioselectivity also plays an important role, particularly for CR rectification. Overall, Aa can be viewed as a molecular rectifier in which cumulative contributions from molecular dynamics and regioselectivity modulate the dipole-induced effects on charge transfer.

RESULTS AND DISCUSSION

Charge-Transfer Processes. To determine whether Aa could rectify charge transfer, we need to compare its ability to mediate charge transfer in which the electron moves toward its C-terminus versus its N-terminus (Chart 1a). For this purpose, we prepared dyads composed of Aa as an electron donor and 1-alkylpyrene (Py) as an electron acceptor. Linking Py either to the C- or the N-terminus of Aa yielded Aa-Py and Py-Aa, respectively (Chart 1b,c). For mixtures of dichloromethane (DCM) and acetonitrile (MeCN) as a solvent media, we estimated that the $\Delta G^{(0)}$ for the photoinduced electron transfer from Aa to Py varied between −0.05 and −0.3 eV, that is, between about 2- and 12-fold of the thermal energy, k_BT (Table 1).

dx.doi.org/10.1021/ja505618n | J. Am. Chem. Soc. 2014, 136, 12966−12973

Table 1. Redox and Charge-Transfer Properties of Aa (an Electron Donor) and Py (an Electron Acceptor) for Various Solvent Media

solvent	v:v	ε^a	n	γ^b	μ/cP^c	$E^{(1/2)}_{Aa^{\bullet+}/Aa}$ V vs SCE^d	$E^{(1/2)}_{mPy/mPy^{\bullet-}}$ V vs SCE^d	E_{00}/eV^e	$\Delta G^{(0)}_{CS}$/eV^f	$\Delta G^{(0)}_{CR}$/eV^f
TCE		8.40	1.4923	0.33	1.5	0.985	−2.26	3.02	−0.021	−3.0
DCM		9.18	1.4241	0.38	0.38	0.957	−2.24	3.03	−0.060	−2.9
DCM + MeCN	3:1	17.9	1.4020	0.45	0.36	0.810	−2.12	3.05	−0.24	−2.8
	1:1	24.8	1.3825	0.48	0.35	0.767	−2.08	3.02	−0.25	−2.8
	1:3	31.2	1.3565	0.51	0.34	0.744	−2.06	3.04	−0.30	−2.7
MeCN		37.6	1.3445	0.53	0.34	0.729	−2.05	3.03	−0.31	−2.7

[a]The dielectric constants were obtained from impedance-spectroscopy measurements.[39,40] [b]Solvent polarity, $\gamma = n-2-\varepsilon-1$. [c]Dynamic viscosity.[39] [d]The half-wave reduction potentials for the different solvents were extrapolated from cyclic voltammetry measurements employing samples with different composition of the electrolyte solutions[41,42] [Aa = 2-hexanamido-*N*-hexyl-5-(piperidin-*N*-yl)benzamide; mPy = 1-methylpyrene]. [e]The values for the zero-to-zero energy were extracted from the crossing points of the normalized absorption and emission spectra of Aa dissolved in the corresponding solvent. [f]The values of $\Delta G(0)$ for the photoinduced charge separation, CS, and for the back charge transfer leading to charge recombination, CR, were estimated using the Rehm−Weller equation.[41,43]

From dielectric studies[39] we determined that Aa has a dipole moment of 6 ± 2 D. Concurrently, we expect that a dyad with Aa as a donor will manifest increased rates of photoinduced charge separation when the electron moves in the same direction as the Aa dipole, which points toward the C-terminus.[10,11] Hence, Aa-Py should manifest larger rates for charge separation than Py-Aa.

To study this behavior, we selectively excite the Aa moiety in the donor−acceptor dyads. The UV absorption of Aa extends to 400 nm, corresponding to the optical transitions to its lowest singlet excited state (see Figure S14 in the Supporting Information). This region of the spectrum is bathochromic with respect to the alkylpyrene bands (Figure 1a),[49,51−56] which allows for selective excitation of the Aa moiety at about 390 to 400 nm. Upon photoexcitation of both dyads in DCM, broad transient-absorption bands appear at about 410 and 710 nm, which is indicative of the formation of the singlet-excited state of the anthranilamide, ^{1}Aa* (Figures 1c and 2a,b). A picosecond growth of transient peaks at 500 and 580 nm accompanies the decay of the ^{1}Aa* absorption (Figure 2a,b). We assign the 500 nm peak to the reduced pyrene,[28,57] $Py^{\bullet-}$, and the 580 nm peak to the radical cation of the anthranilamide, $Aa^{\bullet+}$ (Figure 1b,c).

For each of the investigated samples the transient absorption bands at 500 and 580 nm rise and decay simultaneously. The growth of the bands at 500 and 580 nm, therefore, correspond to the initial photoinduced CS, and the subsequent decay of these radical-ion bands is due to CR (Figure 2d).

Studies employing two-dimensional nuclear magnetic resonance (NMR) spectroscopy eliminated the possibility for "through-space" donor−acceptor interactions (see Supporting Information). Therefore, the observed electron-transfer processes occurred via through-bond pathways mediated by the methylene linkers. Analysis of the electron-transfer rates, using the Marcus−Levich−Jortner formalism, indicated that CS and CR were nonadiabatic processes, consistent with the lack of detectable charge-transfer bands in the ground-state absorption spectra (see Supporting Information).

An increase in the media polarity causes an increase in both the charge-separation and the charge-recombination rate constants, k_{CS} and k_{CR}, respectively (Figure 3a,b).[58] A polar medium stabilizes the zwitterionic charge-transfer states, and, hence, increases the CS driving force, $-\Delta G_{CS}{}^{(0)}$ (Table 1). As expected, this polarity-induced negative shift in $\Delta G_{CS}{}^{(0)}$ increases the observed k_{CS} (Figure 3a). Conversely, the CR kinetics exhibited the opposite trends. The polarity-induced

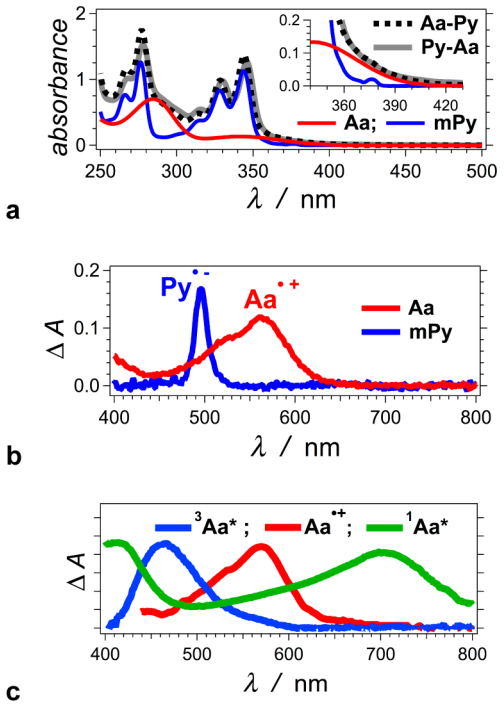

Figure 1. Absorption spectra of the donor−acceptor dyads, and of their components and transients. (a) Steady-state spectra (30 μM in DCM). (b) Spectra from electrochemical measurements recorded at the cathodic and the anodic peak of cyclic voltammograms of Aa and 1-metylpyrene (mPy), respectively (100 mM tetrabutylammonium hexafluorophosphate in MeCN). (c) Absorption spectra of Aa transients recorded using pump−probe spectroscopy (λ_{ex} = 350 nm, 5 μJ per pulse):[47,48] singlet excited state, ^{1}Aa*, recorded at 10 ps after the pulse for DCM solution; triplet excited state, ^{3}Aa*, recorded 2 ns after the pulse for solutions containing 1-bromobutane;[40] radical cation, $Aa^{\bullet+}$, recorded 2 ns after the pulse for aqueous samples of Aa suspended with a surfactant (10 mM odium dodecyl sulfate) and an electron-acceptor cationic fluorescence quencher, 10 mM $CuSO_4$.[49,50]

stabilization of the CT states brings them closer to the ground state, making $\Delta G_{CR}{}^{(0)}$ less negative (Table 1). This polarity-induced decrease in the CR driving force, $-\Delta G_{CR}{}^{(0)}$, accompanies an increase in the observed k_{CR} for both dyads (Figure 3b). Hence, while CS follows the trends of the Marcus normal region, CR occurs in a regime consistent with the Marcus inverted region.[59−61]

Rectification Occurs for Both Charge Separation and Recombination. To quantify the Aa-induced rectification of

dx.doi.org/10.1021/ja505618n | J. Am. Chem. Soc. 2014, 136, 12966−12973

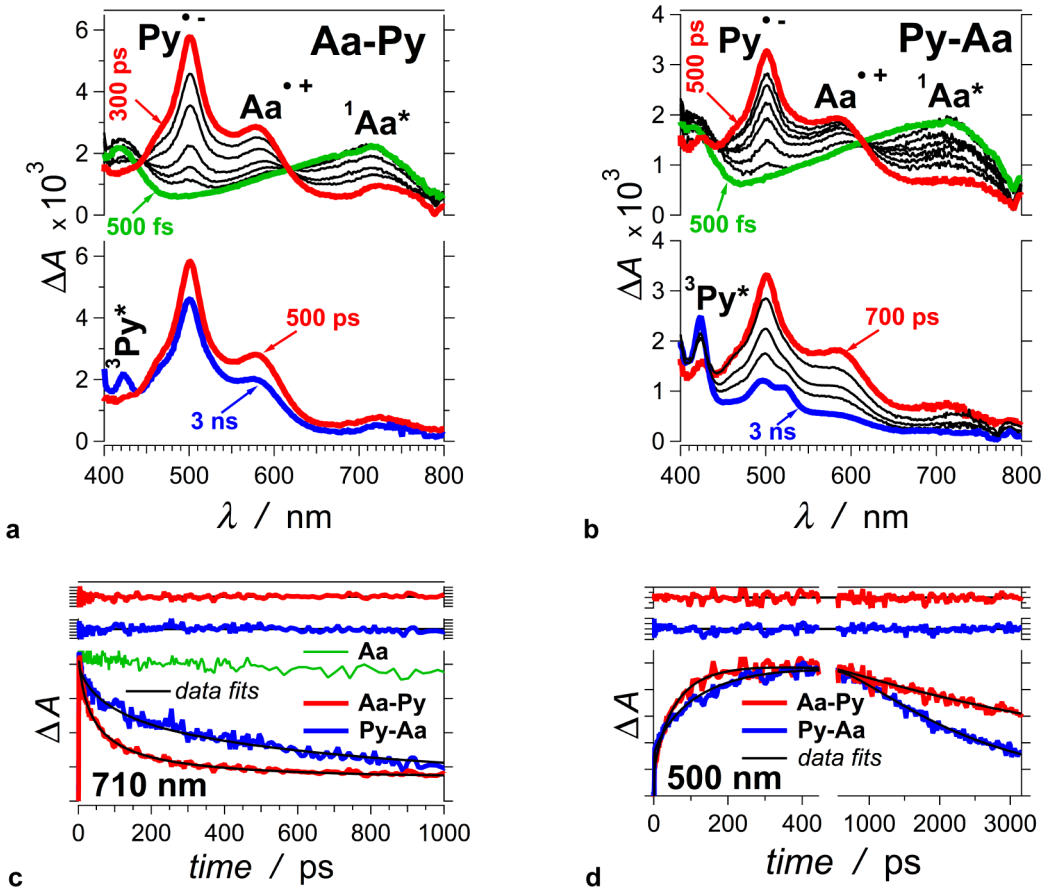

Figure 2. Transient absorption spectra of the donor–acceptor dyads dissolved in DCM (λ_{ex} = 395 nm, 5 μJ per pulse).[47,48] (a, b) Transient absorption spectra of Aa-Py and Py-Aa. (c, d) Transient absorption kinetics of Aa-Py, Py-Aa, and Aa, showing (c) the decays of the Aa singlet-exited state; and (d) the rise and decay of the charge-transfer states, monitored at the absorption peak of the $Py^{\bullet-}$ transient.

the initial photoinduced charge transfer, we compare the CS rates exhibited by the two donor–acceptor dyads. A similar comparison between the rates of the subsequent CR reveals the effect of the orientation of Aa on the deactivation of the charge-transfer state. Indeed, comparing a faster forward photoinduced charge transfer (e.g., CS) with a slower back charge entrainment (e.g., CR) has been occasionally employed for illustrating molecular rectification of donor–acceptor and donor–bridge–acceptor conjugates. Such a definition of rectification, however, is misleading because CS and CR represent different electronic transitions. While CS involves a transition from a locally excited to a charge-transfer state, CR represents the deactivation of the charge-transfer state to the ground state or to comparatively low-lying triplet excited states.[50]

We define the charge-transfer rectification, R, separately for CS and for CR as logarithmic ratios between the rate constants, k, of electron transfer along and against the Aa dipole:

$$R_{CS} = \lg\frac{(k_{CS}(\text{Aa-Py}))}{(k_{CS}(\text{Py-Aa}))} \quad (1a)$$

$$R_{CR} = \lg\left(\frac{k_{CR}(\text{Py-Aa})}{k_{CR}(\text{Aa-Py})}\right) \quad (1b)$$

Because in CS the electron moves toward Py and in CR toward Aa, k_{CS}(Aa-Py) is in the numerator of eq 1a and k_{CR}(Py-Aa) is in the numerator of eq 1b. A value of R = 0 would indicate no rectification, while R = 1 would mean that the rate of the electron transfer along the molecular permanent dipole is an order of magnitude faster than the electron transfer against the dipole. A negative value of R would correspond to electron transfer being faster against the dipole than along it.

For each of the solvent mixtures of DCM and MeCN, k_{CS} for Aa-Py was larger than k_{CS} for Py-Aa (Figure 3a), while k_{CR} for Aa-Py was smaller than k_{CR} for Py-Aa (Figure 3b). As a result, R_{CS} and R_{CR} assumed values between 0.1 and 0.8 (Figure 3c). In other words, charge separation occurs more rapidly in the direction of the dipole moment (i.e., faster in Aa-Py than in Py-Aa), just as expected. Moreover, the positive R_{CR} values indicate that charge recombination behaves similarly, which means that charge recombination is impeded after accelerated charge separation in Aa-Py. While this behavior is desirable for energy-conversion applications, it contradicts the Marcus transition-state theory prediction of a negative R_{CR}.

Varying solvent polarity provides further insights. Increasing polarity decreases R_{CS} (Figure 3c), which suggests that the increased media polarity enhances electrostatic screening and reduces the Aa dipole effect on charge separation. These observations support the notion that the molecular dipoles affect the electron-transfer kinetics by stabilizing or destabilizing the charge-transfer states.[18] In Aa-Py, charge separation moves the electron in the same direction as the intrinsic Aa dipole. The charge-transfer state formed in this manner is oriented against the ground-state dipole (i.e., the positive pole of the Aa dipole points toward the radical anion). This

dx.doi.org/10.1021/ja505618n | J. Am. Chem. Soc. 2014, 136, 12966–12973

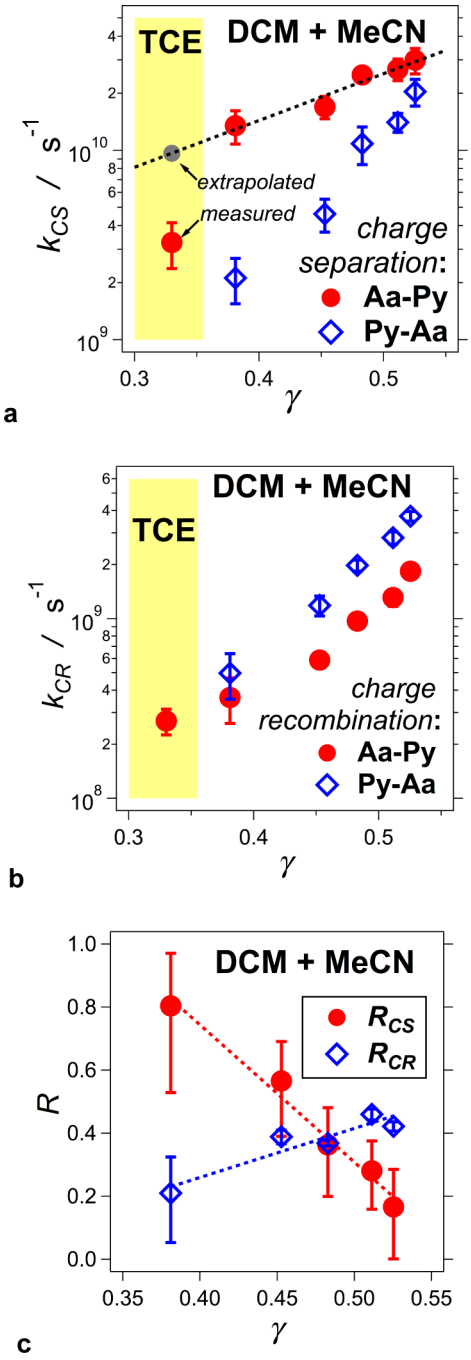

Figure 3. Dependence of charge-transfer kinetics and rectification on the solvent polarity, $\gamma = n^{-2} - \varepsilon^{-1}$. (a, b) Polarity dependence of the rate constants of charge separation (CS) and charge recombination (CR) measured for the two dyads, Aa-Py and Py-Aa (Chart 1b,c), for mixtures of acetonitrile (MeCN) and dichloromethane (DCM) and for 1,1,2,2-tetrachloroethane (TCE). The mixtures of DCM and MeCN correspond to 0%, 25%, 50%, 75%, and 100% (v:v) of MeCN (Table 1). (c) Dependence of the CS and CR rectification (as defined by eq 1a and 1b) on the polarity of the solvent media.

orientation stabilizes the $Aa^{\bullet+}$-$Py^{\bullet-}$ state, causing an increase in the charge separation rate for the relatively small values of $-\Delta G_{CS}^{(0)}$ (Table 1). For Py-Aa, on the other hand, the ground-state dipole is oriented in the same direction as the charge-transfer state, raising its energy, and decreasing the rate of CS.

Conversely, for CR we observed behavior that does not completely agree with the notion of the dipole-induced stabilization and destabilization of the charge-transfer states. Specifically, R_{CR} has a positive value, which increases slightly with the increase in the solvent polarity (Figure 3c). The $\Delta G_{CR}^{(0)}$ values of about −3 eV (Table 1) place the CR processes in the Marcus inverted region.[59−61] Dipole-induced stabilization of the charge-transfer state makes $\Delta G_{CR}^{(0)}$ less negative for Aa-Py, thereby increasing its CR rates. It would, therefore, be expected that $Aa^{\bullet+}$-$Py^{\bullet-}$ should undergo faster CR than $Py^{\bullet-}$-$Aa^{\bullet+}$, resulting in negative values of R_{CR} (eq 1b). Additionally, due to the media screening of the dipole, the increase in solvent polarity should result in a less negative R_{CR} (i.e., in a positive $\Delta R_{CR}/\Delta\gamma$ slope where R_{CR} is negative for nonpolar solvents and approaches zero as the media polarity increases).

The positive slope, $\Delta R_{CR}/\Delta\gamma$, and the positive values of R_{CR} indicate simultaneous contributions of polarity-dependent and polarity-independent factors to the CR kinetics. While the dipole effects depend on the polarity of the media, intramolecular factors, such as the donor−acceptor electronic coupling, should be practically solvent independent, as our theoretical studies suggest. For example, donor−acceptor coupling in $Py^{\bullet-}$-$Aa^{\bullet+}$, which is larger than that in $Aa^{\bullet+}$-$Py^{\bullet-}$, opposes the expected dipole effect. If such a difference between the couplings is large enough, it can surpass the dipole effect and make R_{CR} positive even in the least polar solvent. Therefore, as the solvent polarity increases, the dipole effect decreases, making R_{CR} more positive.

Alternatively, one might attribute the positive R_{CR} values to the triplet manifolds in the charge recombination pathways. Upon the decay of the radical ions in a relatively nonpolar medium, we observed the formation of a pyrene triplet state, ^{3}Py*, as revealed by transient-absorption bands at 422, 490, and 523 nm that became apparent upon the CR (Figure 2a,b).[62,63] Increasing the media polarity, however, decreased the relative amplitude of the ^{3}Py* transient absorption bands. Furthermore, even though no triplet formation was observed in MeCN (see Figure S4 in the Supporting Information), the value of R_{CR} for MeCN is still positive (γ = 0.53, Figure 3c). Therefore, charge recombination pathways involving triplet states cannot account for the positive shifts in R_{CR}.

Conformational Dynamics is Particularly Important for Charge Separation. Although the NMR studies results suggest that the Aa-Py structures do not fold (see Supporting Information), conformational dynamics do still appear to play a role in the donor−acceptor coupling and charge-transfer kinetics. Evidence for the impact of molecular dynamics on the charge-transfer processes comes from the data fits to the transient-absorption kinetics. Monoexponential functions could not provide acceptable data fits for the rise of the radical-ion transients when DCM and MeCN were used as solvents. Hence, we extracted the CS rate constants from multi-exponential data fits.[64] Such heterogeneous kinetics is characteristic for electron-transfer systems, in which flexible linkers provide the coupling between the donor and the acceptor.[20,64] The multiexponential character of the CS kinetics suggests that the initial photoinduced electron transfer from ^{1}Aa* to Py involves more than one conformer. While the rotation around the σ-bonds between Aa and Py does not bring the two aromatic moieties in contact with each other, the conformational dynamics of the locally excited states in the dyads is essential for the observed trends of CS and R_{CS}.

On the other hand, the charge-recombination behavior was quite different. The radical-ion decay traces exhibit mono-

dx.doi.org/10.1021/ja505618n | J. Am. Chem. Soc. 2014, 136, 12966−12973

exponential character for all solvents. This finding indicates that the conformational relaxation dynamics of the CT states is significantly faster than the measured CR rates. The CR processes, therefore, likely originate from thermally relaxed conformer populations. Electrostatic interactions of the Aa dipole with the CT states, which are oppositely oriented for the two dyads, would hypothetically steer the relaxation of $Aa^{\bullet+}$-$Py^{\bullet-}$ and $Py^{\bullet-}$-$Aa^{\bullet+}$ to different conformers with different donor–acceptor coupling. A population of thermally relaxed $Aa^{\bullet+}$-$Py^{\bullet-}$ conformers with donor–acceptor coupling stronger than the coupling in the most abundant $Py^{\bullet-}$-$Aa^{\bullet+}$ conformers can potentially account for the positive values observed for R_{CR}.

If molecular dynamics is the underlying cause for these CS and CR trends, an increase in the media viscosity should affect the observed charge-transfer kinetics.[65,66] To examine such viscosity dependence, we employed 1,1,2,2-tetrachloroethane (TCE) as a solvent medium. TCE is about 4 times more viscous than any of the mixtures of DCM and MeCN we used (Table 1). Also, TCE is a non-hydrogen bonding solvent with a polarity and polarizability close to those of DCM.

Upon photoexcitation, both dyads mediated charge separation when dissolved in the viscous TCE solvent. Only for Aa-Py, however, was the buildup of the $Aa^{\bullet+}$ and $Py^{\bullet-}$ radical ions sufficient to reliably evaluate the charge-transfer kinetics. In contrast to the multiexponential kinetics of radical-ion formation observed for DCM and MeCN, the charge-separation kinetics in TCE exhibit a monoexponential character. Furthermore, the measured k_{CS} for Aa-Py in TCE is about one-third the value expected from the polarity dependence of k_{CS} for the mixtures of DCM and MeCN (Figure 3a). This finding is consistent with the hypothesis that the increased solvent viscosity suppresses molecular motions, making it harder to access the ^{1}Aa*-Py conformers that enable efficient photoinduced charge separation via improved donor–acceptor electronic coupling. It follows then that the rates of conformational sampling of the locally excited dyads and of charge separation are comparable in media composed of DCM and MeCN.

Conversely, the viscosity of the media does not appear to affect the observed CR for Aa-Py. The measured value of k_{CR} for TCE follows the polarity-dependence trend that we recorded for the mixtures of DCM and MeCN (Figure 3b); i.e., slowing down the molecular dynamics of the CT state of the dyad does not have a major effect on the charge recombination.

Regioselectivity Also Contributes to the Charge-Transfer Rectification. Density functional theory (DFT) and time-dependent DFT (TDDFT) calculations for Aa at the B3LYP/6-311+G(d,p)[67−69] level provide insight into the regioselectivity of CT and how it impacts the charge-transfer rectification. TDDFT calculations for the 25 lowest states in a DCM or MeCN polarizable continuum solvent model predict absorption spectra in good agreement with the experimental one (see Figure S14 in the Supporting Information), providing some validation for the model. The errors relative to the experimental spectrum lie well within the few tenths of an eV accuracy (which maps to a few tens of nanometers here) typically expected for valence excited states in TDDFT.[70]

The lowest singlet excited state S_1 is predicted to occur at 353 nm in DCM. This excitation, which corresponds to a HOMO–LUMO transition, is the state accessed experimentally with 400 nm radiation. As shown in the natural transition orbitals (Figure 4a), the vertical excitation shifts electron

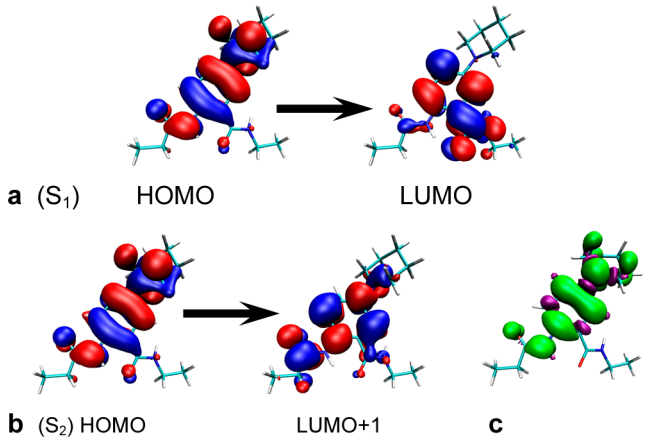

Figure 4. Natural transition orbitals[75] for (a) the S_1 and (b) S_2 states at the ground state geometry of Aa with truncated aliphatic chains. The S_1 state is dominated by a HOMO–LUMO transition, while the S_2 state is primarily a HOMO–LUMO + 1 transition. (c) Electron spin density of the radical cation, $Aa^{\bullet+}$; green, excess spin up (i.e., radical cation); and purple, excess spin down.

density from the piperidinyl ring toward the C-terminus amide bond. Subsequent geometric relaxation on the S_1 excited state surface alters the conformation of the piperidinyl ring, while the rest of the structure remains nearly unchanged (see Figure S10a in the Supporting Information). The geometric relaxation does not significantly alter the character of the LUMO orbital that becomes singly occupied in the S_1 state (see Supporting Information). Interestingly, the relaxed S_1 structure is nearly identical to that of the Aa radical cation (see Figure S10b in the Supporting Information). As noted earlier, these results suggest that the excitation and subsequent charge transfer do not significantly affect the geometry in the amide bond region.

The second-lowest singlet excited state is predicted at 294 nm in DCM. Although the experiments here did not involve this state, it provides an interesting contrast to the S_1 state. Whereas the S_1 excitation steers electron density toward the C-terminus amide, the S_2 vertical excitation involves a HOMO to LUMO + 1 transition that shifts the electron density toward the N-terminus amide bond (Figure 4b). Relaxation on the S_2 excited state surface once again primarily alters the piperidinyl ring conformation, but here it adopts a geometry with the piperidinyl ring perpendicular to the plane of the rest of the molecule. This conformation is typical of twisted intramolecular charge-transfer (TICT) states,[71] and it differs significantly from that of the relaxed S_1 state.

Performing the same the calculations in polarizable continuum MeCN or in the gas phase (no continuum solvent model) has minimal impact on the predicted structures and the character of the excited states; e.g., the vertical excitation wavelengths change by less than 10 nm. While continuum-solvent models cannot capture the sometimes important local solute–solvent interactions, the polarizable continuum model should adequately capture the bulk electrostatic and polarization interactions that likely dominate the effects in these aprotic solvents. Moreover, the predicted insensitivity to the solvent is consistent with the absence of any experimentally observed solvent effect on E_{00} for Aa (Table 1). The predicted structures, excited-state characters, and excitation energies are also robust with respect to the choice of density functional (B3LYP vs PBE0)[72] and the basis set (6-31G(d)[73,74] vs 6-

dx.doi.org/10.1021/ja505618n | J. Am. Chem. Soc. 2014, 136, 12966−12973

311+G(d,p)), providing further confidence in the predictions (see Supporting Information for details).

These computational results suggest that regioselectivity contributes to the observed charge rectification. Photoexcitation to the S_1 state shifts electron density toward the C-terminus amide in the Aa donor, which improves the electronic coupling to the Py acceptor when the Py moiety is linked to the C-terminus (as in Aa-Py). This leads to faster charge separation rates for Aa-Py than for Py-Aa.

Conversely, these calculations predict that the Aa structures and excited state character depend minimally on the solvent polarity, which contrasts the pronounced solvent effect on R_{CS} observed experimentally (Figure 3c). Thus, the charge separation rectification depends more strongly on the dipole effect than on the regioselective electronic coupling that is dictated by the positioning of the linker relative to the piperidinyl ring.

Indeed, previous studies have shown that charge-transfer regioselectivity associated with the position of donor−acceptor linkers is more important for charge recombination than for the initial photoinduced charge separation.[76] Charge recombination will involve the singly occupied molecular orbital (SOMO) on the Aa radical cation, which is very similar to the Aa ground state HOMO and which extends over the N-terminus amide (Figure 4c). Hence, charge-recombination kinetics should be faster for Py-Aa than for Aa-Py, as was observed experimentally (Figures 2 and 3), leading to a positive value of R_{CR}. However, the lack of solvent dependence for the Aa radical cation SOMO cannot account for the positive $\Delta R_{CR}/\Delta\gamma$ slope observed in the experiments. Hence, while regioselectivity can help explain the positive sign of R_{CR}, the polarity dependence of R_{CR} likely arises from dipole effects on charge recombination.

In summary, the observed rectification of charge separation can largely be attributed to the electric dipole effect, which depends on media polarity. Regioselectivity plays a smaller role in charge separation. Conversely, regioselectivity appears to be more important for the rectification of charge recombination, though the electric dipole contributions also play a role.

CONCLUSIONS

This study demonstrates that an anthranilamide rectifies both the forward and the back charge transfer. The magnitude of rectification induced by only a single Aa residue is comparable to the rectifying effects reported for polypeptide helices composed of more than 10 amino acids. This charge-transfer rectification is governed by the permanent dipole moment of the Aa residue, as evident from its dependence on solvent polarity. In addition to the dipole-induced differentiation between the energy levels of oppositely oriented charge-transfer states,[18] the conformational dynamics and regioselectivity offer alternative avenues for modulating the field-induced rectification. The charge separation occurs at a relatively small driving force, and the charge recombination that follows occurs in the regime of the Marcus inverted region. The positive values of R_{CR} and R_{CS} indicate for systems designs for impeding charge recombination while improving the facility of photinduced charge separation. These features set paradigms that are essential for energy conversion and nanoelectronics.

ASSOCIATED CONTENT

Supporting Information

Experimental methods, including synthesis and characterization of the Aa derivatives, and spectroscopic and electrochemical techniques used; electron-transfer analysis; and details for the computational work. This material is available free of charge via the Internet at http://pubs.acs.org.

AUTHOR INFORMATION

Corresponding Authors

gregory.beran@ucr.edu
vullev@ucr.edu

Present Addresses

[⊥]PrimusLabs, Santa Maria, CA 93455, United States.
[#]Department of Cell Biology, Harvard Medical School, Boston, MA 02115, United States, and Program in Cellular and Molecular Biology, Boston Children's Hospital, Boston, MA 02115, United States.
[▽]GlaxoSmithKline, MDR-Boston, Waltham, MA 02451, United States.

Notes

The authors declare no competing financial interest.

ACKNOWLEDGMENTS

Funding for this work was from the National Science Foundation (CBET 0935995, CBET 0923408, and DBI 0731660, as well as GRFP 2011081805 for V.N. and IGERT DGE 0903667 for J.M.L), and from the City of Riverside, CA, as well as from NSF grants CHE-1112568 and CHE-1362465, and supercomputer time from XSEDE (TG-CHE110064) for the theoretical studies (G.J.O.B. and J.D.H.), is gratefully acknowledged.

REFERENCES

(1) Aviram, A.; Ratner, M. A. *Chem. Phys. Lett.* **1974**, *29*, 277−283.
(2) Heath, J. R. *Annu. Rev. Mater. Res.* **2009**, *39*, 1−23.
(3) Heath, J. R.; Ratner, M. A. *Phys. Today* **2003**, *56*, 43−49.
(4) Metzger, R. M. *Chem. Rev.* **2003**, *103*, 3803−3834.
(5) Ding, W.; Negre, C. F. A.; Palma, J. L.; Durrell, A. C.; Allen, L. J.; Young, K. J.; Milot, R. L.; Schmuttenmaer, C. A.; Brudvig, G. W.; Crabtree, R. H.; Batista, V. S. *ChemPhysChem* **2014**, *15*, 1138−1147.
(6) Sayed, S. Y.; Fereiro, J. A.; Yan, H. J.; McCreery, R. L.; Bergren, A. J. *Proc. Natl. Acad. Sci. U.S.A.* **2012**, *109*, 11498−11503.
(7) Heath, J. R.; Ratner, M. A. *Phys. Today* **2003**, *56*, 43−49.
(8) Pedersen, K. S.; Bendix, J.; Clerac, R. *Chem. Commun.* **2014**, *50*, 4396−4415.
(9) Layfield, R. A. *Organometallics* **2014**, *33*, 1084−1099.
(10) Xia, B.; Bao, D.; Upadhyayula, S.; Jones, G.; Vullev, V. I. *J. Org. Chem.* **2013**, *78*, 1994−2004.
(11) Ashraf, M. K.; Pandey, R. R.; Lake, R. K.; Millare, B.; Gerasimenko, A. A.; Bao, D.; Vullev, V. I. *Biotechnol. Prog.* **2009**, *25*, 915−922.
(12) Doyle Declan, A. *Eur. Biophys. J.* **2004**, *33*, 175−179.
(13) Doyle, D. A.; Cabral, J. M.; Pfuetzner, R. A.; Kuo, A. L.; Gulbis, J. M.; Cohen, S. L.; Chait, B. T.; MacKinnon, R. *Science* **1998**, *280*, 69−77.
(14) Dutzler, R.; Campbell, E. B.; Cadene, M.; Chait, B. T.; MacKinnon, R. *Nature* **2002**, *415*, 287−294.
(15) Doig, A. J. *Biophys. Chem.* **2002**, *101−102*, 281−293.
(16) Wada, A. *Adv. Biophys.* **1976**, *9*, 1−63.
(17) Hol, W. G. J. *Adv. Biophys.* **1985**, *19*, 133−165.
(18) Shin, Y.-G. K.; Newton, M. D.; Isied, S. S. *J. Am. Chem. Soc.* **2003**, *125*, 3722−3732.
(19) Galoppini, E.; Fox, M. A. *J. Am. Chem. Soc.* **1996**, *118*, 2299−2300.
(20) Fox, M. A.; Galoppini, E. *J. Am. Chem. Soc.* **1997**, *119*, 5277−5285.
(21) Yasutomi, S.; Morita, T.; Imanishi, Y.; Kimura, S. *Science* **2004**, *304*, 1944−1947.

(22) Mandal, H. S.; Kraatz, H. B. *Chem. Phys.* **2006**, *326*, 246−251.
(23) Gao, J. A.; Muller, P.; Wang, M.; Eckhardt, S.; Lauz, M.; Fromm, K. M.; Giese, B. *Angew. Chem., Int. Ed.* **2011**, *50*, 1926−1930.
(24) Chaudhry, B. R.; Wilton-Ely, J. D. E. T.; Tabor, A. B.; Caruana, D. J. *Phys. Chem. Chem. Phys.* **2010**, *12*, 9996−9998.
(25) Kise, K. J.; Bowler, B. E. *Inorg. Chem.* **2003**, *42*, 3891−3897.
(26) Morita, T.; Kimura, S.; Kobayashi, S.; Imanishi, Y. *J. Am. Chem. Soc.* **2000**, *122*, 2850−2859.
(27) Garbuio, L.; Antonello, S.; Guryanov, I.; Li, Y.; Ruzzi, M.; Turro, N. J.; Maran, F. *J. Am. Chem. Soc.* **2012**, *134*, 10628−10637.
(28) Knorr, A.; Galoppini, E.; Fox, M. A. *J. Phys. Org. Chem.* **1997**, *10*, 484−498.
(29) Giese, B.; Wang, M.; Gao, J.; Stoltz, M.; Muller, P.; Graber, M. *J. Org. Chem.* **2009**, *74*, 3621−3625.
(30) Metzger, R. M.; Chen, B.; Hopfner, U.; Lakshmikantham, M. V.; Vuillaume, D.; Kawai, T.; Wu, X. L.; Tachibana, H.; Hughes, T. V.; Sakurai, H.; Baldwin, J. W.; Hosch, C.; Cava, M. P.; Brehmer, L.; Ashwell, G. J. *J. Am. Chem. Soc.* **1997**, *119*, 10455−10466.
(31) Sek, S.; Swiatek, K.; Misicka, A. *J. Phys. Chem. B* **2005**, *109*, 23121−23124.
(32) Sek, S.; Misicka, A.; Swiatek, K.; Maicka, E. *J. Phys. Chem. B* **2006**, *110*, 19671−19677.
(33) Shlizerman, C.; Atanassov, A.; Berkovich, I.; Ashkenasy, G.; Ashkenasy, N. *J. Am. Chem. Soc.* **2010**, *132*, 5070−5076.
(34) Mayo, S. L.; Ellis, W. R., Jr.; Crutchley, R. J.; Gray, H. B. *Science* **1986**, *233*, 948−952.
(35) Gray, H. B.; Winkler, J. R. *Proc. Natl. Acad. Sci. U.S.A.* **2005**, *102*, 3534−3539.
(36) Vullev, V. I.; Jones, G., II. *Res. Chem. Intermed.* **2002**, *28*, 795−815.
(37) Jones, G., II; Vullev, V.; Braswell, E. H.; Zhu, D. *J. Am. Chem. Soc.* **2000**, *122*, 388−389.
(38) Odonnell, J. F.; Mann, C. K. *J. Electroanal. Chem.* **1967**, *13*, 157−162.
(39) Upadhyayula, S.; Bao, D.; Millare, B.; Sylvia, S. S.; Habib, K. M. M.; Ashraf, K.; Ferreira, A.; Bishop, S.; Bonderer, R.; Baqai, S.; Jing, X.; Penchev, M.; Ozkan, M.; Ozkan, C. S.; Lake, R. K.; Vullev, V. I. *J. Phys. Chem. B* **2011**, *115*, 9473−9490.
(40) Hu, J.; Xia, B.; Bao, D.; Ferreira, A.; Wan, J.; Jones, G.; Vullev, V. I. *J. Phys. Chem. A* **2009**, *113*, 3096−3107.
(41) Bao, D.; Millare, B.; Xia, W.; Steyer, B. G.; Gerasimenko, A. A.; Ferreira, A.; Contreras, A.; Vullev, V. I. *J. Phys. Chem. A* **2009**, *113*, 1259−1267.
(42) Bao, D.; Ramu, S.; Contreras, A.; Upadhyayula, S.; Vasquez, J. M.; Beran, G.; Vullev, V. I. *J. Phys. Chem. B* **2010**, *114*, 14467−14479.
(43) Rehm, D.; Weller, A. *Isr. J. Chem.* **1970**, *8*, 259−271.
(44) Gray, H. B.; Winkler, J. R. *Annu. Rev. Biochem.* **1996**, *65*, 537−561.
(45) Vullev, V. I. *J. Phys. Chem. Lett.* **2011**, *2*, 503−508.
(46) Kapetanaki, S. M.; Ramsey, M.; Gindt, Y. M.; Schelvis, J. P. M. *J. Am. Chem. Soc.* **2004**, *126*, 6214−6215.
(47) Nuñez, V.; Upadhyayula, S.; Millare, B.; Larsen, J. M.; Hadian, A.; Shin, S.; Vandrangi, P.; Gupta, S.; Xu, H.; Lin, A. P.; Georgiev, G. Y.; Vullev, V. I. *Anal. Chem.* **2013**, *85*, 4567−4577.
(48) Guo, S.; Bao, D.; Upadhyayula, S.; Wang, W.; Guvenc, A. B.; Kyle, J. R.; Hosseinibay, H.; Bozhilov, K. N.; Vullev, V. I.; Ozkan, C. S.; Ozkan, M. *Adv. Funct. Mater.* **2013**, *23*, 5199−5211.
(49) Vullev, V. I.; Jones, G. *Tetrahedron Lett.* **2002**, *43*, 8611−8615.
(50) Jones, G., II; Vullev, V. I. *Org. Lett.* **2002**, *4*, 4001−4004.
(51) Yoshinaga, T.; Hiratsuka, H.; Tanizaki, Y. *Bull. Chem. Soc. Jpn.* **1977**, *50*, 3096−3102.
(52) Dierksen, M.; Grimme, S. *J. Chem. Phys.* **2004**, *120*, 3544−3554.
(53) Vullev, V. I.; Jiang, H.; Jones, G., II. *Top. Fluoresc. Spectrosc.* **2005**, *10*, 211−239.
(54) Jones, G., II; Vullev, V. I. *J. Phys. Chem. A* **2001**, *105*, 6402−6406.
(55) Jones, G., II; Vullev, V. I. *Org. Lett.* **2001**, *3*, 2457−2460.
(56) Jones, G., II; Lu, L. N.; Vullev, V.; Gosztola, D.; Greenfield, S.; Wasielewski, M. *Bioorg. Med. Chem. Lett.* **1995**, *5*, 2385−2390.
(57) Getoff, N.; Solar, S.; Richter, U. B.; Haenel, M. W. *Radiat. Phys. Chem.* **2003**, *66*, 207−214.
(58) Wan, J.; Ferreira, A.; Xia, W.; Chow, C. H.; Takechi, K.; Kamat, P. V.; Jones, G.; Vullev, V. I. *J. Photochem. Photobiol., A* **2008**, *197*, 364−374.
(59) Suppan, P. *Top. Curr. Chem.* **1992**, *163*, 95−130.
(60) Grampp, G. *Angew. Chem., Int. Ed.* **1993**, *32*, 691−693.
(61) Marcus, R. A. *Annu. Rev. Phys. Chem.* **1964**, *15*, 155−196.
(62) Porter, G.; Windsor, M. W. *Proc. R. Soc. London, Ser. A* **1958**, *245*, 238−258.
(63) Heinzelmann, W.; Labhart, H. *Chem. Phys. Lett.* **1969**, *4*, 20−24.
(64) Jones, G., II; Zhou, X.; Vullev, V. I. *Photochem. Photobiol. Sci.* **2003**, *2*, 1080−1087.
(65) Jones, G., II; Yan, D.; Hu, J.; Wan, J.; Xia, B.; Vullev, V. I. *J. Phys. Chem. B* **2007**, *111*, 6921−6929.
(66) Vasquez, J. M.; Vu, A.; Schultz, J. S.; Vullev, V. I. *Biotechnol. Prog.* **2009**, *25*, 906−914.
(67) Becke, A. D. *J. Chem. Phys.* **1993**, *98*, 5648−5652.
(68) Lee, C. T.; Yang, W. T.; Parr, R. G. *Phys. Rev. B* **1988**, *37*, 785−789.
(69) Krishnan, R.; Binkley, J. S.; Seeger, R.; Pople, J. A. *J. Chem. Phys.* **1980**, *72*, 650−654.
(70) Leang, S. S.; Zahariev, F.; Gordon, M. S. *J. Chem. Phys.* **2012**, *136*, 104101.
(71) Grabowski, Z. R.; Rotkiewicz, K.; Rettig, W. *Chem. Rev.* **2003**, *103*, 3899−4031.
(72) Adamo, C.; Barone, V. *J. Chem. Phys.* **1999**, *110*, 6158−6170.
(73) Hehre, W. J.; Ditchfie, R.; Pople, J. A. *J. Chem. Phys.* **1972**, *56*, 2257−2261.
(74) Harihara, P. C.; Pople, J. A. *Theor. Chim. Acta* **1973**, *28*, 213−222.
(75) Martin, R. L. *J. Chem. Phys.* **2003**, *118*, 4775−4777.
(76) Thompson, A. L.; Ahn, T. S.; Thomas, K. R. J.; Thayumanavan, S.; Martinez, T. J.; Bardeen, C. J. *J. Am. Chem. Soc.* **2005**, *127*, 16348−16349.

Dipole-Mediated Rectification of Intramolecular Photoinduced Charge Separation and Charge Recombination (Supporting Information)

Duoduo Bao,[†,⊥] Srigokul Upadhyayula,[†,‡,#] Jillian M. Larsen,[†] Bing Xia,[†,▽] Boriana Georgieva,[†] Vicente Nuñez,[†] Eli M. Espinoza,[§] Joshua D. Hartman,[§] Michelle Wurch,[†] Andy Chang,[†] Chung-Kuang Lin,[†] Jason Larkin,[†] Krystal Vasquez,[§] Gregory J. O. Beran,*[,§] and Valentine I. Vullev*[,†,‡,§,∥]

[†]Department of Bioengineering, [‡]Department of Biochemistry, [§]Department of Chemistry, and [∥]Materials Science and Engineering Program, University of California, Riverside, CA 92521, U.S.A.
Present addresses: [⊥]PrimusLabs, Santa Maria, CA 93455, U.S.A. [#]Department of Cell Biology, Harvard Medical School, Boston, MA 02115, U.S.A., and Program in Cellular and Molecular Biology, Boston Children's Hospital, Boston, MA 02115, U.S.A.
[▽]GlaxoSmithKline, MDR-Boston, Waltham, MA 02451, U.S.A.

Materials. 5-fluoro-2-nitrobenzoic acid **(1),** 1-methylpyrene, mPy (Figure S1b), piperidine, 1-pyreneacetic acid, 1-pyrenemethyl-amine hydrochloride, and hexanoic anhydride were purchased from TCI America. Tin (II) chloride dihydrate ($SnCl_2 \cdot 2\ H_2O$), *N,N'*-Diisopropylcarbodiimide (DIC, 99%), *N*-hydroxysuccinimide (NHS, 98%), N,N-diisopropylethylamine (DIPEA, 99.5%), 1-[*bis*(dimethylamino) methylene]-1H-1,2,3-triazolo[4,5-b]pyridinium-3-oxid hexafluorophosphate (HATU), 1-hydroxy-7-azabenzotriazole (HOAt), triethylamine (Et_3N), hexylamine, and ethylenediamine-tetraacetic acid (EDTA) were purchased from Sigma-Aldrich. All other reagents (including HPLC grade, spectroscopic grade and anhydrous solvents) were purchased from Fisher Scientific.

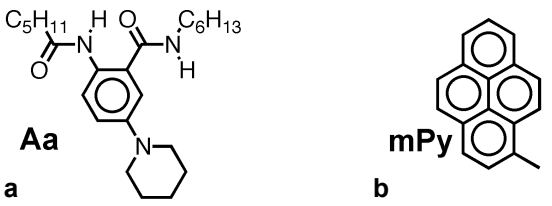

Figure S1. Structural formulae of the control compounds used for characterizing the donor and acceptor properties. **(a)** Alkyl-terminated single residue for hole-transfer electrets, 2-hexanamido-*N*-hexyl-5-(piperidin-*N*-yl)benzamide (Aa). **(b)** auxiliary electron acceptor, 1-methylpyrene (mPy).

General synthesis information **(Figure S2).** Proton (^{1}H) NMR spectra were recorded at 400 MHz at ambient temperature using degassed $CDCl_3$ as solvent. ^{13}C NMR spectra were recorded at 100 MHz at ambient temperature with $CDCl_3$ as solvent. Chemical shifts are reported in parts per million relative to $CDCl_3$ (^{1}H, δ 7.241; ^{13}C, δ 77.23). Data for ^{1}H NMR are reported as follows: chemical shift, integration, multiplicity (s = singlet, d = doublet, t = triplet, q = quartet, p = pentaplet/quintet, m = multiplet), integration and coupling constants. All ^{13}C NMR spectra were recorded with complete proton decoupling.

High-resolution mass-spectra were obtained on a Q-TOF mass spectrometer. Analytical thin layer chromatography was performed using 0.25 mm silica gel 60-F plates. Flash chromatography was performed using 60 Å, 32−63 μm silica gel. Yields refer to chromatographically and spectroscopically pure materials, unless otherwise stated. All reactions were carried out in oven-dried glassware under an argon or nitrogen atmosphere.

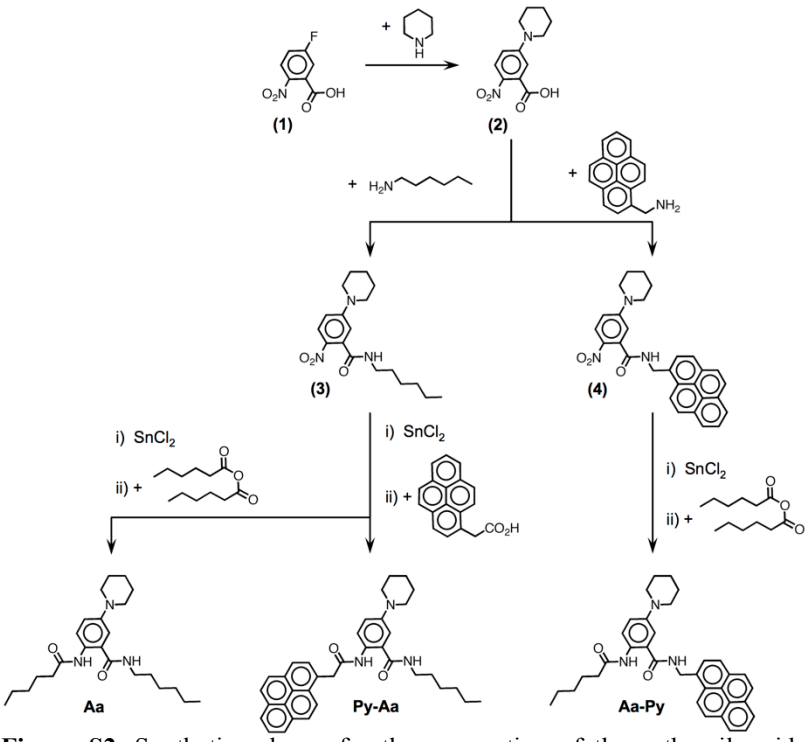

Figure S2. Synthetic scheme for the preparation of the anthranil-amide derivatives. Nucleophilic aromatic substitution for (**2**). Amide coupling for (**3**) and (**4**). Selective reduction of the nitro group, immediately followed by amide coupling for the final products, Aa, Py-Aa, and Aa-Py.

2-nitro-5-(piperidin-N-yl)benzoic acid **(2)**. 2-nitro-5-fluoro-benzoic acid (1) (1.9 g, 10 mmol) and piperidine (12 ml, 12 mmol) were mixed in a 25 ml flask equipped with a water-cooled condenser and

immersed in a temperature-controlled oil bath. The mixture was refluxed at 108 ^{o}C for 4 h. After cooling to room temperature, the reaction solution was diluted with 100 mL DCM, and washed with 1 M HCl (100 ml × 3) and with brine (100 ml × 3). The organic layer was collected, dried over Na_2SO_4, and concentrated *in vacuo* to produce yellow powder (1.7 g, 6.6 mmol, 66%) of 2-nitro-5-(piperidin-1-yl)benzoic acid (2): ^{1}H-NMR (400 MHz, $CDCl_3$) δ/ppm: 8.00 (1 H, d, J = 9.6 Hz), 6.92 (1 H, d, J = 2.8 Hz), 6.83 (1 H, dd, J_1 = 9.6 Hz, J_2 = 2.8 Hz), 3.46 (4 H, s), 1.69 (6 H, s); ^{1}H-NMR (400 MHz, DMSO-d_6) δ/ppm: 13.34 (1 H, s), 7.91 (1 H, d, J = 9.6 Hz), 6.97 (1 H, dd, J_1 = 9.6 Hz, J_2 = 3.0 Hz), 6.91 (1 H, d, J = 3.0 Hz), 3.46 (4 H, t, J_1 = 6 Hz, J_2 = 4.8 Hz), 1.58 (2 H, m), 1.52 (4 H, m); HRMS m/z calculated for $C_{13}H_{15}N_2O_6$ (M + HCOO) 295.0928, found 295.0936 (M + HCOO).

***N-hexyl-2-nitro-5-(piperidin-N-yl)benzamide* (3).** DIC (1.0 ml, 6.4 mmol) was added to 10 ml ice-chilled DMF solution of (**2**) (950 mg, 3.8 mmol) and NHS (870 mg, 7.6 mmol). The mixture was stirred at 0 ^{o}C for 2 h. Hexylamine (1.5 ml, 11 mmol) was added drop-wise, and the solution was stirred at 0 ^{o}C for additional 0.5 h. The reaction mixture was poured into 100 ml 1 M HCl, and yellow precipitate formed. The precipitate was collected by filtration, and washed. The wet solid was dissolved in 50 ml DCM, dried over Na_2SO_4, and the DCM was removed under reduced pressure to produce yellow solid. Purification using flash chromatography (stationary phase: silica gel; eluent gradient: from 100 % hexanes to 50 % ethyl acetate in hexanes) afforded 875 mg yellow powder (2.6 mmol, 69% yield) of *N*-hexyl-2-nitro-5-(piperidin-1-yl)benzamide (3): ^{1}H-NMR (400 MHz, $CDCl_3$) δ/ppm: 8.03 (1 H, d, J = 9.6 Hz), 6.94 (1 H, dd, J_1 = 9.6 Hz, J_2 = 2.0 Hz), 6.89 (1 H, d, J = 2.0 Hz), 5.73 (1 H, s), 3.43 (4 H, s), 1.74 (4 H, s), 1.67 (2 H, m), 1.61 (2 H, t, J = 7.2 Hz), 1.37 (2 H, m), 1.33 (6 H, m), 0.875 (3 H, t, J = 6.8 Hz); HRMS m/z calculated $C_{18}H_{28}N_3O_3$ (M + H) 334.2125, found 334.2161 (M + H).

***2-nitro-5-(piperidin-N-yl)-N-(pyren-1-ylmethyl)benzamide* (4).** HATU (1.9 g, 5 mmol) and DIPEA (5.1 ml, 31 mmol), dissolved in 10 ml DMF, were added to 10 ml DMF solution of (**2**) (1.0 g, 4.0 mmol), 1-pyrenemethylamine hydrochloride (1.6 g, 6.0 mmol) and HOAt (2.2 g, 16 mmol). After stirring it at room temperature for 4 h, the mixture solution was poured in 100 ml DI water and yellow precipitate formed. The precipitate was collected dissolved in DCM to form a dark brown solution. It was dried with Na_2SO_4, and concentrated *in vacuo*, which caused the formation of yellow precipitate. The precipitate was collected and dried to produce 1.7 g (90% crude yield) of yellow substance (with limited solubility in many organic solvents), which was used directly for the synthesis of Py-Aa. 52 mg of the crude product were purified using flash chromatography (stationary phase: silica gel; eluent gradient: from 100 % hexanes to 100 % ethyl acetate in hexanes) to afford 45 mg (87% column yield) of bright yellow powder of (N-(pyrenyl)acethyl-2-nitro-5-(piperidin-1-yl)benzamide (4): ^{1}H-NMR (400 MHz, DMSO-d_6) δ/ppm: 9.07 (1 H, t, J = 5.4 Hz), 8.45 (1 H, d, J = 9.2 Hz), 8.30 (1 H, d, J = 7.6 Hz), 8.26 (3 H, m), 8.14 (2 H, s; 1 H, d, J = 7.6 Hz), 8.05 (1 H, t, J = 7.6 Hz), 7.92 (1 H, d, J = 9.6 Hz), 6.95 (1 H, dd, J_1 = 9.6 Hz, J_2 = 2.6 Hz), 6.81 (1 H, d, J = 2.6 Hz), 5.15 (2 H, d, J = 5.6 Hz), 3.42 (4 H, t, J_1 = 5.6 Hz, J_2 = 4.8 Hz), 1.56 (2 H, m), 1.50 (4 H, m); HRMS m/z calculated for $C_{29}H_{26}N_3NaO_3$ (M + Na), 486.1788, found 487.1783 (M + Na).

***N-hexyl-5-(piperidin-N-yl)-2-(2-(pyren-1-yl)acetamido)benzamide* (Py-Aa).** Tin (II) chloride dihydrate (850 mg, 3.8 mmol) and (**3**) (210 mg, 0.63 mmol) were mixed in 2 ml ethanol and refluxed for 4 h. After the reduction was completed (as monitored using TLC) the ethanol was evaporated *in vacuo* to yield white pasty solid. The remaining solid was immediately blanked with nitrogen. The product from the reduction of (**3**), 2-amino-*N*-hexyl-5-(piperidin-1-yl)benzamide, was confirmed with HRMS, m/z calculated $C_{18}H_{30}N_3O$ (M + H) 304.2383, found 304.2386 (M + H), and used for the next coupling step without further purification. 1-pyreneacetic acid (250 mg, 0.95 mmol), HOAt (350 mg, 2.5 mmol), and HATU (570 mg, 1.5 mmol) were dissolved in 5 ml DMF and added to the reduced solid under nitrogen, followed by dropwise addition of DIPEA (810 µl, 4.9 mmol). The solution was kept under inert atmosphere and stirred at room temperature for 8 h. The reaction mixture was added to 300 ml aqueous saturated solution of $NaHCO_3$ and extracted with 100 ml DCM. The DCM solution was washed with saturated solution $NaHCO_3$ (100 ml × 4), and with 5 mM solution of EDTA (300 ml × 3). The organic layer was dried over Na_2SO_4, and concentrated *in vacuo* to produce oily substance. Purification using flash chromatography (stationary phase: silica gel; eluent gradient: from 100 % hexanes to 50 % ethyl acetate in hexanes) afforded 190 mg white powder (0.35 mmol, 55% yield). ^{1}H-NMR (400 MHz, $CDCl_3$) δ/ppm: 10.28 (1H, s), 8.31 (1 H, d, J = 9.2 Hz), 8.30 (1 H, d, J = 9.1 Hz), 8.20 (1 H, d, J = 7.8 Hz), 8.15 (1 H, d, J = 7.5 Hz), 8.14 (1 H, d, J = 7.6 Hz), 8.08 (1 H, d, J = 9.2 Hz), 8.06 (1 H, d, J = 12.6 Hz), 8.04 (2 H, d, J = 8.64), 7.97 (1 H, t, J = 7.6 Hz), 6.95 (1 H, dd, J_1 = 9.2 Hz, J_2 = 2.8 Hz), 6.78 (1 H, d, J = 2.8 Hz), 5.78 (1 H, t, J = 4.5 Hz), 4.41 (2 H, s), 2.99 (4 H, t, J = 5.3 Hz), 2.79 (2 H, q, J = 6.5 Hz), 1.65 (4 H, p, J = 5.6 Hz), 1.50 (2 H, d, J = 5.8 Hz), 1.14 (8 H, m), 0.86 (3 H, t, J = 7.3 Hz); ^{13}C-NMR (100 MHz, $CDCl_3$) δ/ppm: 169.77, 168.77, 148.32, 131.54, 131.17, 131.06, 130.91, 129.97, 128.90, 128.15, 127.74, 127.37, 126.08, 125.43, 125.37, 125.34, 125.24, 124.96, 123.70, 123.56, 122.92, 120.42, 114.75, 51.41, 43.76, 39.79, 31.54, 29.30, 26.66, 25.96, 24.21, 22.75, 14.24; HRMS m/z calculated for $C_{36}H_{40}N_3O_2$ (M + H) 546.3115, found 546.3114 (M + H).

***2-hexanamido-5-(piperidin-N-yl)-N-(pyren-1-ylmethyl)benzamide* (Aa-Py).** Tin (II) chloride dihydrate (1.35 g, 6 mmol) and crude (**4**) (470 mg, 1.0 mmol) were mixed in 25 ml ethanol and refluxed for 6 h. After the reduction was completed (as monitored using TLC) the ethanol was evaporated *in vacuo*. The remaining solid was immediately blanked with nitrogen and dissolved in 8 ml DMF at room temperature while purging with the inert gas. The product of the reduction of (**4**), 2-amino-5-(piperidin-1-yl)-*N*-(pyren-1-ylmethyl)benzamide, was confirmed with HRMS, m/z calculated $C_{29}H_{28}N_3O$ (M + H) 434.2232, found 434.2211 (M + H). Hexanoic anhydride (860 µl, 4 mmol) and Et_3N (210 µl, 1.5 mmol) were added to the nitrogen-purged DMF solution and it was stirred at room temperature for 6 h. The reaction mixture was added to 300 ml aqueous saturated solution of $NaHCO_3$ stirred with 100 ml DCM. The formed precipitate was removed by filtration and the organic phase was collected. The DCM solution was further washed with saturated $NaHCO_3$ (100 ml × 2). The organic layer was dried over Na_2SO_4, and concentrated *in vacuo* to produce oily substance. Purification using flash chromatography (stationary phase: silica gel; eluent gradient: from 100 % hexanes to 50 % ethyl acetate in hexanes) afforded 200 mg white powder (0.37 mmol, 37% yield, based on the crude starting material). ^{1}H-NMR (400 MHz, $CDCl_3$) δ/ppm: 10.49 (1 H, s), 8.34 (1 H, d, J = 9.1 Hz), 8.28 (1 H, d, J = 9.2 Hz), 8.20 (2 H, d, J = 7.6 Hz), 8.15 (1 H, d, J = 7.8 Hz) , 8.14 (1 H, d, J = 9.2 Hz), 8.07 (1 H, d, J = 13.2 Hz), 8.05 (1 H, d, J = 13.2 Hz), 8.02 (1 H, t, J = 7.6 Hz) , 8.01 (1 H, d, J = 7.8 Hz), 6.95 (1 H, dd, J_1 = 9.1 Hz, J_2 = 2.8 Hz), 6.88 (1 H, d, J = 2.8 Hz), 6.62 (1 H, t, J = 5.0 Hz), 5.29 (2 H, d, J = 5.2 Hz), 2.92 (4 H, t, J_1 = 5.5 Hz, J_2 = 5.3 Hz), 2.34 (2 H, t, J = 7.8 Hz), 1.70 (2 H, p, J = 7.5 Hz), 1.56 (4 H, p, J = 5.6 Hz), 1.44 (2 H, p, J = 5.8 Hz), 1.33 (4 H, m), 0.89 (3 H, t, J = 6.9 Hz); ^{13}C-NMR (100 MHz, $CDCl_3$) δ/ppm: 172.06, 169.13, 148.03, 131.97, 131.64, 131.45, 130.92, 130.49, 129.33, 128.68, 127.97, 127.54, 127.43, 126.44, 125.81, 125.70, 125.31, 125.06, 124.90, 123.12, 122.82, 122.09, 121.32, 115.14, 51.54, 42.71, 38.54, 31.65, 25.89, 25.60, 24.10, 22.67, 14.23; HRMS m/z calculated for $C_{35}H_{38}N_3O_2$ (M + H) 532.2959, found 532.2979 (M + H).

***2-hexanamido-N-hexyl-5-(piperidin-N-yl)benzamide* (Aa).** Tin (II) chloride dihydrate (3.6 g, 16 mmol) and (**3**) (890 mg, 2.7 mmol) were mixed in 2 ml ethanol and refluxed for 4 h. After the reduction was completed (as monitored using TLC), the ethanol was evaporated *in vacuo*. The remaining solid was immediately blanked with nitrogen and dissolved in 2 ml DMF at room temperature while purging with the inert gas. Hexanoic anhydride (1.4 ml, 6.2 mmol) and Et_3N (580 µl, 4 mmol) were added to the nitrogen-purged DMF solution and it was stirred at room temperature for 6 h. The reaction mixture was added to 300 ml aqueous saturated solution of $NaHCO_3$ and extracted with 100 ml DCM. The DCM solution was washed with saturated solution $NaHCO_3$ (100 ml × 4), and with 5 mM solution of EDTA (300 ml × 3). The organic layer was dried over Na_2SO_4, and concentrated *in vacuo* to produce white oily substance. Purification using flash chromatography (stationary phase: silica gel; eluent gradient: from 100 % hexanes to 25 % ethyl acetate in hexanes) afforded 590 mg white powder (1.4 mmol, 52% yield). ^{1}H-NMR (400 MHz, $CDCl_3$) δ/ppm: 10.48 (1H, s), 8.40 (1H, d, J = 9.1 Hz), 7.05 (1H, dd, J_1 = 9.1 Hz, J_2 = 2.7 Hz), 7.01 (1H, d, J = 2.7 Hz), 6.15 (1H, s), 3.39 (2H, td, J_1 = 7.2 Hz, J_2 = 5.9 Hz), 3.08 (4H, t, J = 5.4 Hz), 2.34 (2H, t, J = 7.4 Hz), 1.72 (6H, m), 1.57 (4H, m), 1.32 (10H, m), 0.88 (3H, t, J = 7.0 Hz), 0.87 (3H, t, J = 7.0 Hz); ^{13}C-NMR (100 MHz, $CDCl_3$) δ/ppm: 171.89, 169.32, 147.44, 131.76, 122.54, 122.35, 120.56, 115.44, 51.49, 40.14, 38.39, 31.57, 31.46, 29.49, 26.78, 25.75, 25.47, 24.00, 22.65, 22.48, 14.10, 14.03; HRMS m/z calculated for $C_{24}H_{39}N_3O_2$ (M) 401.3042, found 401.3033 (M).

The charge transfer primarily occurs via through-bond coupling. We investigate whether the charge-transfer processes can occur via through-bond or through-space pathways. The methylene linker between the donor and acceptor introduces conformational flexibility into the dyad. This flexibility could potentially modulate the CR rates in two distinct manners: (1) through conformational gating,[1-3] resulting from relaxation of the CT states of the two dyads to conformers with different donor-acceptor coupling; and (2) via formation of folded conformers, in which through-space contact between the donor and the acceptor provide alternative CT pathways.

Despite this conformational freedom, we did not detect proximity between the donor and the acceptor in the dyads. The through-space correlations between the protons in the dyads, as revealed by nuclear Overhauser effect spectroscopy (NOESY), are consistent with extended structures in which both amides adopt *trans* conformations (Figure S3). The anthranilamide protons exhibit NOE correlations only with the piperidinyl hydrogens, *pp*1, closest to the aromatic ring and with the non-hydrogen-bonded amide proton, *am*2 (Figure S3a-c). The proton of the hydrogen-bonded amide, *am*1, correlates only with the protons of the closest hexanoyl methylene, *h*2, in Aa-Py (Figure S3c), and only with the protons of the methylene donor-acceptor linker, *me*, in Py-Aa (Figure S3d). The pyrene protons show NOE correlation only with one another and with the *me* hydrogens of the donor-acceptor linker (Figure S3e-g).

Indeed, the NMR analysis pertains to the ground electronic state. We employed density functional theory (DFT) and time-dependent DFT (TDDFT) calculations on the Aa moiety to examine the behavior of the neutral ground state, its radical cation, and the lowest-lying singlet excited states. In all cases, relaxing the geometry does not significantly alter

the structure in the amide bond region (Figure S10). This implies that neither photoexcitation nor single-electron oxidation of Aa perturbs the relatively rigid structure in the amide-bond regions of the dyads. Together, the NMR and computational data suggest that the dyads do not adopt folded conformations that would create spatial overlap between donor and acceptor. Therefore, the principle charge-transfer pathway likely involves through-bond rather than through-space donor-acceptor coupling.

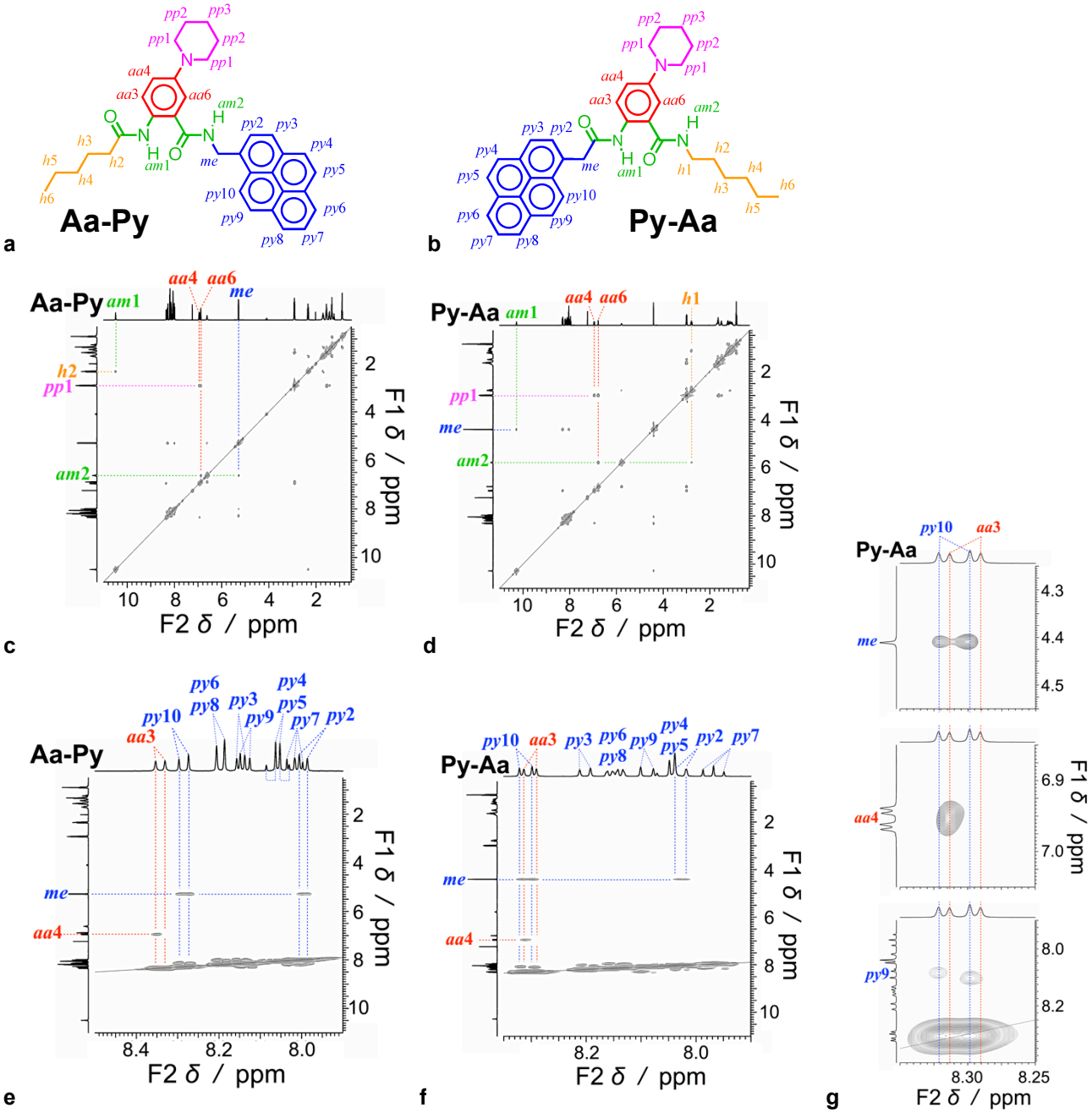

Figure S3. Nuclear Overhauser effect spectroscopy (NOESY) of Aa-Py and Py-Aa (5 mM in degassed $CDCl_3$). **(a,b)** Chemical structures of the dyads with labels of the protons and color designation of the different molecular regions: Aa – red, Py and the methylene linkers (*me*) – blue, amides (*am*) – green, hexyl and hexanoyl (*h*) – orange, and piperidinyls (*pp*) – violet. **(c,d)** NOESY spectra of the dyads with some of the through-space correlation between protons from different molecular regions. **(e,f)** NOESY spectra of the dyads with expanded Py regions along F2. The chemical shifts of the pyrene protons were assigned based on ^{1}H correlation spectroscopy (COSY) and on the ^{1}H-^{1}H coupling constants, *J*. The pyrene protons correlated through-space only with the protons of the methylene linker, *me*. **(g)** NOESY spectra of Py-Aa with the region of the overlapping chemical shifts of *py*10 and *aa*3 expanded along F2. The off-diagonal signals reveal that *py*10 correlates through-space only with *me* and *py*9; and *aa*3 – only with *aa*4.

Electrochemical measurements. Cyclic voltammetry was conducted using Reference 600^{TM} Potentiostat/Galvanostat/ZRA (Gamry Instruments, PA, U.S.A.), equipped with a three-electrode cell, as previously described.[4] The half-wave reduction potentials, $E^{(1/2)}$, of Aa$^{\bullet+}$ and mPy were measured using electrolyte solutions with different dielectric constants, ε.[4] From the dependence of $E^{(1/2)}$ on $(1 - \varepsilon^{-1})$ we estimated the effective radii[5] of Aa (0.26 nm) and mPy (0.31 nm), and extrapolated the reduction half-wave potentials of the analytes for the different neat solvents and solvent mixtures (Table 1).[4,5] For spectroelectrochemical measurements, the three-electrode cell was assembled in a 10-mm×10-mm quartz cuvette, the bottom 5 mm of which narrowed to 2-mm×10-mm. UV/visible light source and a CCD spectrometer were connected with the cuvette holder via optical fibers. The working electrode, platinum mesh, was placed in the 2-mm×10-mm confined section of the cuvette and the light beam was aligned to pass through the mesh ensuring 2-mm optical path length. Platinum and silver wires were used for a counter and pseudoreference electrodes, respectively. The latter was calibrated with ferrocene samples. The intensities, $I(E)$, of the light passing through the sample and the working electrode were recorded at different potentials, E, while swiping the voltage. The change in the absorbance, ΔA, for each potential, corresponding to the spectra of the electrochemically formed oxidized or reduced species, was calculated in respect with the intensity at 0 V vs. the reference, $\Delta A(E) = \log(I(0) / I(E))$.

Solvent characterization. The static dielectric constants of the solvents and the solvent mixtures (ε, Table 1) were determined using impedance measurements that employed three-terminal capacitance sample cell connected to an ultrahigh precision Wheatstone bridge, incorporated in a HP 4284A LCR meter.[6] The refractive indices (n, Table 1) were measured with Spectronic Instruments Refractometer model 334610.[5] The sample densities were evaluated with a Densito 30PX portable densitometer (Mettler Toledo, Columbus, OH, USA)[6]. The kinematic viscosity of each of the solvents and the solvent mixtures was estimated with a capillary U-tube Cannon-Fenske N 956 Size 150 viscometer and, using the measured densities, converted to dynamic viscosity (μ, Table 1).[7]

UV/visible absorption and emission spectroscopy. Steady-state absorption spectra were recorded in a transmission mode using a JASCO V-670 spectrophotometer (Tokyo, Japan); and steady-state emission spectra were measured, also in a transmission mode, with a FluoroLog-3 spectrofluorometer (Horiba-Jobin-Yvon, Edison, NJ, USA) as previously reported.[8]

Transient absorption spectroscopy. The transient-absorption spectra (Figure S4) were recorded in transmission mode with 2-mm quartz cuvettes using a Helios pump-probe spectrometer (Ultrafast Systems, LLC, Florida, USA) equipped with a delay stage allowing maximum probe delays of 3.2 ns at 7 fs temporal step resolution.[9] Immediately prior the measurements, all samples were purged with argon. The laser source for the Helios was a SpitFire Pro 35F regenerative amplifier yielding (Spectra Physics, Newport, CA, USA) generating 800-nm pulses (>35 fs, 4.0 mJ, at 1 kHz).[10] The amplifier was pumped with an Empower 30 Q-switched laser ran at 20 W. A MaiTai SP oscillator provided the seed beam (55 nm bandwidth).[10] The wavelength of the pump was tuned using an optical parametric amplifier, OPA-800CU (Newport Corporation, Newport, CA, USA), equipped with a signal second and forth harmonic generators.[9] For optimal OPA performance, the pulse duration from the amplifier was tuned to 50 fs. The signal was tuned to 1,580 nm for the Aa-Py and Py-Aa samples, and to 1,400 nm for the Aa samples. The power of the signal and the idler prior the second harmonic generator was stabilized at about 150 mW.

The measured kinetic curves, i.e., ΔA_λ vs. t (Figure S5), following the rise and decay of the radical-ion transients were fit with multiexponential functions:

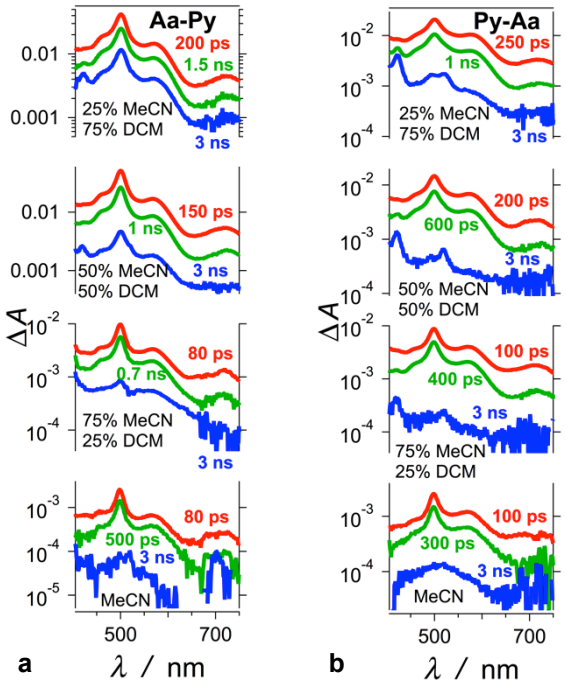

Figure S4. Transient absorption spectra of the dyads in various mixtures of DCM and MeCN showing the decay of the radical ions ploted against logarithmic ordinates. The increase in content MeCN suppressed the formation of ^{3}Py* (peak at about 420 nm) upon CR. (λ_{ex} = 395 nm, 5 μJ per pulse).

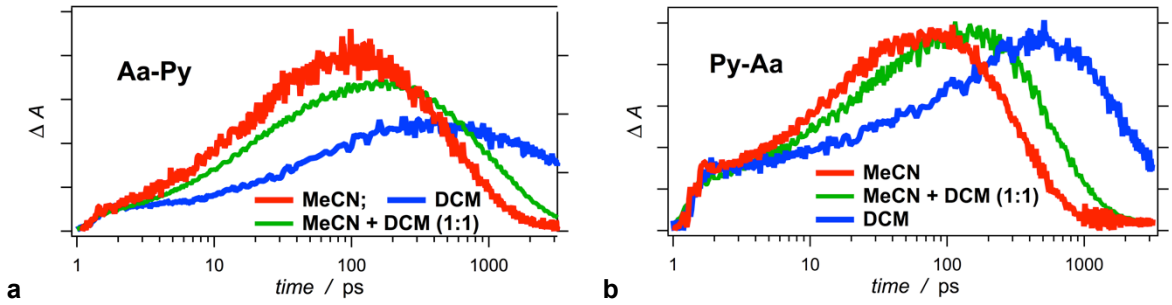

Figure S5. Transient absorption kinetic traces of the donor-acceptor dyads for various solvent media, monitor at 500 nm representing the formation and the decay of the charge-transfer state. The logarithmic representation of the abscissa allows for visualizing the kinetics in a wide time-domain range. (Initial time, t_0, was set at 1 ps; λ_{ex} = 395 nm; 5 μJ per pulse.)

$$\Delta A_\lambda(t) = -\sum_i \alpha_i e^{-k_i^{(r)}(t-t_0)} + \alpha_d e^{-k^{(d)}(t-t_0)} \tag{S1}$$

A Gaussian distribution of the exponential terms along the logarithmic values of the rate constants is representative of electron-transfer kinetics between donor and acceptor coupled through a flexible linker.[11-13] Thus, for the pre-exponential coefficient, α_i, we used an expression for such a distribution around $k_0^{(r)}$, with maximum amplitude α_0:[11]

$$\alpha_i = \alpha_0 \exp\left(-\left(\frac{\lg\left(k_i / k_0^{(r)}\right)}{\Delta_{\lg k}}\right)^2\right) \tag{S2}$$

The central rise rate constants were used for quantifying the CS kinetics, $k_{CS} = k_0^{(r)}$;[11] and the decay rate constants – for the CR kinetics, $k_{CR} = k^{(d)}$. The growth of the radical-ion transients, measured for the Aa-Py samples dissolved in TCE, was successfully fit to a monoexponential rise function, yielding a single $k^{(r)}$ value, which we equated with k_{CS}.

Charge-transfer kinetics. The semiclassical Marcus-Levich-Jortner formalism provides insight into the features of the donor-acceptor systems that govern the electron-transfer rate constants, k_{ET}:[14-16]

$$k_{ET} = \frac{2\pi}{\hbar} H_{if}^2 \frac{\exp(-S_C)}{\sqrt{4\pi\lambda_m k_B T}} \sum_{j=0}^{\infty} \frac{S_C^j}{j!} \exp\left(-\frac{\left(\Delta G_{ET}^{(0)} + \lambda_m + jh\nu_C\right)^2}{4\lambda_m k_B T}\right) \tag{S3}$$

Where H_{if} represents the electronic coupling between the initial and the final state, i.e., between the locally excited and the charge-transfer state for CS, and between the charge-transfer and the ground (or the Py triplet) state for CR. The vibrational-coupling for the transition between the two electronic states is expressed in terms of the electron-transfer driving force, $\Delta G_{ET}^{(0)}$, the Huang-Rhys factor, S_C, and the outer-sphere reorganization energy, λ_m, which for non-coordination conjugates can also be refereed as the media reorganization energy. $S_C = \lambda_i / h\nu_C$, where λ_i is the inner-sphere reorganization energy, ν_C is the average frequency of the high-energy vibrational modes, k_B is the Boltzmann constant and T is the temperature. The media reorganization energy is expressed in terms of the effective radii of donor and the acceptor, r_{Aa} and r_{Py}, and of the center-to-center distance between them, R_{DA}:[17]

$$\lambda_m = \frac{(\Delta e)^2}{4\pi\varepsilon_0}\gamma\left(\frac{1}{2r_{Aa}} + \frac{1}{2r_{Py}} - \frac{1}{R_{DA}}\right) \tag{S4}$$

The term in front of the parentheses represents the contribution to the solvation energy from the transition of Δe electron charges to form a non-equilibrium polarized system,[17] defining a pertinent index for solvent polarity, $\gamma = n^{-2} - \varepsilon^{-1}$.

We have sufficient information to estimate $\Delta G_{ET}^{(0)}$ of CS and CR, and λ_m for the solvent media we used (Table 1). We, however, had to vary the other four parameters in eq. S3 within physically potentially feasible ranges: i.e., λ_i from 0.2 to 0.6 eV, $h\nu_C$ from 0.1 to 0.3 eV, H_{if} from 0.005 to 0.05 eV, and R_{DA} from 6 to 11 Å (Figure S6). We determined that eq. S4 tends to overestimate the magnitude of λ_m. That is, for the examined ranges of parameters, the calculated λ_m is large enough to place $\Delta G_{CS}^{(0)}$ further away from the tip of the Marcus curve (k_{ET} vs. $\Delta G_{ET}^{(0)}$) than $\Delta G_{CR}^{(0)}$, producing CR faster than CS, which was contrary to what we observe for these charge-transfer dyads. Therefore, we used a reduced value for λ_m in eq. S3, $\lambda'_m = 0.5\ \lambda_m$. A possible reason for the overestimated values of λ_m produced from eq. S4 can be sought in the solvation details of the donor and acceptor moieties. In the dyads, the donor and the acceptor share the same solvation cavity, i.e., the solvation media does not completely surround the donor and the acceptor individually.

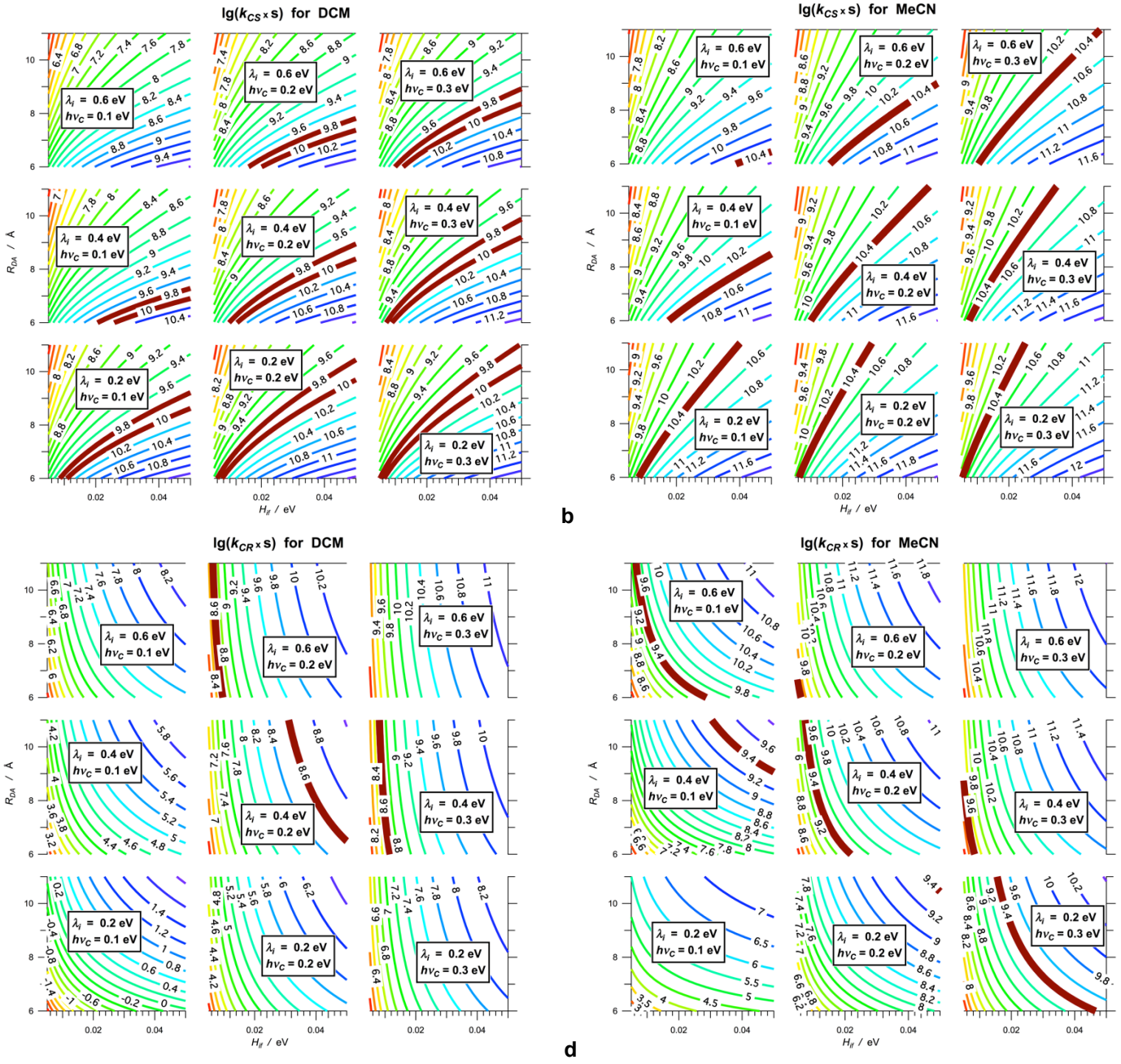

Figure S6. Rate constants of electron transfer between Aa and Py calculated using the Marcus-Levich-Jortner formalism (eq. S3). **(a,b)** CS and **(c,d)** CR rates constants for **(a,c)** DCM and **(b,d)** MeCN where four parameters were varied: R_{DA}, H_{if}, λ_i and $h\nu_C$; and j = 0 to 100 was used. The logarithmic values of the rate constants are represented as contour plots showing the dependence on R_{DA} and H_{if}. The thick brown lines represent the contour levels corresponding to the measured rate constants averaged for Py-Aa and Aa-Py.

For the two of the neat solvent media, DCM and MeCN, we compare the calculated CS and CR rate constants (using eq. S3) with the experimentally measured values, averaged for Py-Aa and Aa-Py (Figure S6). To simplify the search for trends in the calculated results, we assume that the solvent effects on λ_i, $h\nu_C$, H_{if}, and R_{DA} are not substantial. Thus, multidimensional plots should readily reveal a set of conditions where changing only the two media parameters (ε and n) produces rate constants that match the experimental values for both, DCM and MeCN.

For CS, a decrease in H_{if} (to about 005 to 0.02 eV) and a decrease in R_{DA} to less than 8 Å provide quite a reasonable agreement between the calculated and the experimental values of the rate constants (compare the thick brown lines on Figures S4a and S4b). Indeed, this CS trend is lost when λ_i increases to 0.6 eV, and $h\nu_C$ decreases to 0.1 eV. Although the decrease in R_{DA} appears to improve the agreement with the experimental data, we cannot assume R_{DA} values smaller than 5 Å or even 6 Å because it would result in strong NOE NMR cross-correlational peaks, which we did not observe.

For CR such an agreement between the values of the rate constants for DCM and MeCN is apparent only for λ_i = 0.6eV and $h\nu_C$ = 0.2 eV, and for λ_i = 0.4 eV and $h\nu_C$ = 0.3 eV, when H_{if} < 0.01 eV (Figure S6c, d). Also, the CR trends tend to be less sensitive to R_{DA} (Figure S6c, d) probably because the manner in which R_{DA} affects both, λ_m and $\Delta G_{ET}^{(0)}$.

The relatively small electronic coupling, H_{if} < 20 meV, where the MeCN and DCM predicted k_{CS} and k_{CR} agree the best with the experimental measurements, indicates for non-adiabatic regime of the electron-transfer processes. This trend agrees well with the notion for through σ-bond CT pathways (based on the NMR analysis). In the Marcus semi-classical formalism, $H_{if} = H_{if}^{(0)} \exp(-\beta r_{D\text{-}A}/2)$, $H_{if}^{(0)}$ represents the electronic coupling when the donor and the acceptor are in direct contact, and β is an empirical rate falloff parameter with the through-bond donor-acceptor distance, $r_{D\text{-}A}$. Considering β of about 1 Å^{-1}, typical for alkene chains, and $r_{D\text{-}A}$ of about 3 Å for the two linker bonds, H_{if} ranging from 5 to 20 meV corresponds to $H_{if}^{(0)}$ ranging between about 20 and 90 meV.

The trends indicated that the plausible λ_i values for CS were smaller than these for CR. For CR, only λ_i of about 0.4 eV and larger resulted in rate constant that showed agreement with the experimental values. Also, for CR, $h\nu_C$ has to be 0.2 eV or larger to provide plausible rate constant values (Figure S6c , d).

The large gradients of k_{CS} and k_{CR} along the H_{if} direction within the experimentally feasible range of parameters suggest for pronounced sensitivity of the measured rates to the electronic coupling between Aa and Py. Therefore, slight conformational changes would lead to detectable differences in the measured rate constants, which is consistent with the observed heterogeneity in k_{CS} and the discrepancies in the CR kinetics.

Computational methods. The Aa moiety was modeled using (time-dependent) density functional theory. For simplicity, the aliphatic chains on each amide were truncated two carbons beyond the amide (Figure S7). The DFT and TDDFT calculations were performed at the B3LYP/6-311+G(d,p) level[18-20] using a pruned (99,590) "ultrafine" integration grid, as implemented in Gaussian 09.[21] The structures of Aa in the neutral ground state, in the S_1 excited state, the S_2 excited state, and the radical cation were all optimized separately. Spin-unrestricted calculations were used for the radical cation calculations. Solvent effects were estimated by comparing the results from gas-phase calculations to those in an integral equation formalism polarizable continuum model[22] with parameters corresponding to dichloromethane or acetonitrile. Natural transition orbital analysis[23] was used to examine the character of the excited states. The single pair of natural transition orbitals shown here in each case provide a good representation of the excitation, with occupation numbers of 0.95 or higher. Finally, to test the sensitivity of the predictions to the model chemistry, additional calculations were performed in the 6-31G(d) basis[24,25] and with the PBE0 functional.[26] As discussed below, changing the basis and or functional does not alter any of the fundamental conclusions presented in the main article.

The next three sections provide information associated with the theoretical calculations described in the main article. In particular, the results presented here demonstrate that the excitation energies, the optimized structures, and the character of the excitation are suitably converged in the B3LYP/6-311+G(d,p) density functional and basis set used here and that they do not depend too strongly on the solvent environment. All calculations utilized a slightly truncated version of the Aa molecule with shortened alkyl groups shown below.

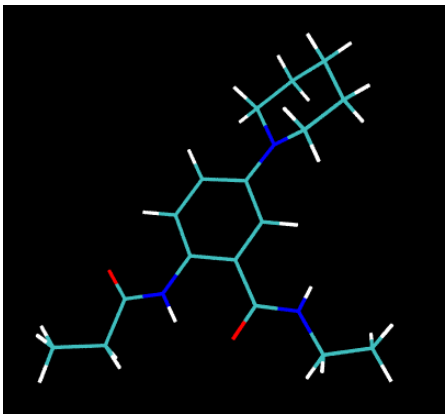

Figure S7. Model of Aa with truncated aliphatic chains used for the calculations described here.

Table S1. Vertical and adiabatic excitation energies for the two lowest singlet excited states in the Aa moiety. Changing the theoretical method and/or solvent does not significantly alter the excitation energies.

Solvent	State S_1		State S_2	
	Vertical	Adiabatic	Vertical	Adiabatic
	B3LYP/6-311+G(d,p)			
Gas	3.52	3.05	4.34	3.96
DCM	3.51	2.91	4.22	3.84
MeCN	3.52	2.88	4.21	3.81
	B3LYP/6-31G(d)			
Gas	3.65	3.14	4.54	4.06
DCM	3.58	3.00	4.41	3.95
MeCN	3.54	2.98	4.31	3.93
	PBE0/6-31G(d)			
Gas	3.78	3.26	4.68	4.23
DCM	3.72	3.11	4.48	4.16
MeCN	3.75	3.09	4.54	4.12

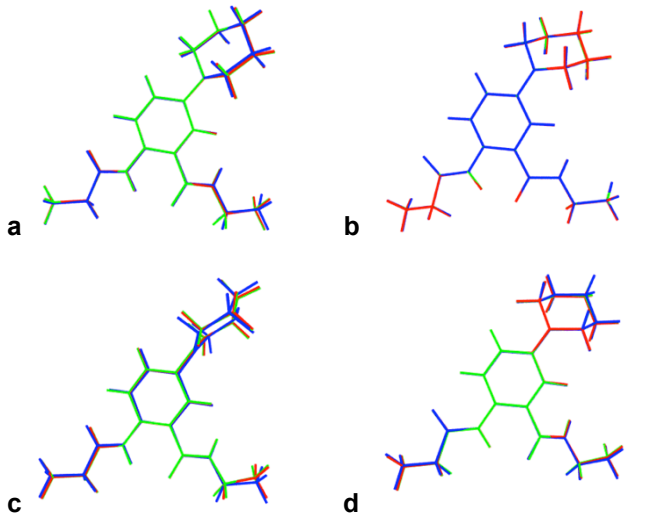

Figure S8. Structure overlays showing the minor effects of the continuum solvation model environments on the optimized geometries of the various species: blue = gas phase, red = in DCM, and green = in MeCN: **(a)** ground state, S_0; **(b)** excited state, S_1; **(c)** excited state, S_2; **(d)** radical cation.

Table S2. Leading orbital amplitude contribution to the S_1 excited state. The character of the excitation is minimally altered in different solvent environments and or theoretical methods.

Solvent	Character	Amplitude
	B3LYP/6-311+G(d,p)	
Gas	HOMO $\longrightarrow$ LUMO	0.693
DCM	HOMO $\longrightarrow$ LUMO	0.693
MeCN	HOMO $\longrightarrow$ LUMO	0.692
	B3LYP/6-31G(d)	
Gas	HOMO $\longrightarrow$ LUMO	0.693
DCM	HOMO $\longrightarrow$ LUMO	0.694
MeCN	HOMO $\longrightarrow$ LUMO	0.693
	PBE0/6-31G(d)	
Gas	HOMO $\longrightarrow$ LUMO	0.692
DCM	HOMO $\longrightarrow$ LUMO	0.696
MeCN	HOMO $\longrightarrow$ LUMO	0.697

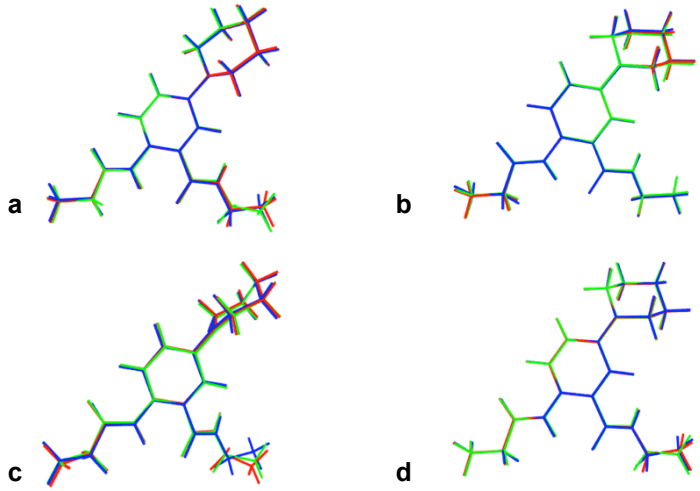

Figure S9. Structure overlays showing the minor effects of the density functional and basis set on the optimized geometries of the various species in DCM solvent: blue = B3LYP/6-311+G(d,p), red = B3LYP/6- 31G(d), and PBE0/6-31G(d): **(a)** ground state, S_0; **(b)** excited state, S_1; **(c)** excited state, S_2; **(d)** radical cation.

TDDFT excitation energies. The excitation energies for the two lowest singlet states of Aa were computed using TDDFT using two different basis sets (6-31G(d) vs. 6-311+G(d,p)) and density functionals (B3LYP vs. PBE0) in each of three different polarizable continuum solvent environments (gas, dichloromethane and acetonitrile). Vertical excitation energies were computed as the difference in the excitation at the ground state geometry computed at the same level of theory and in the same solvent environment. Adiabatic excitation energies were computed as the difference between the ground state and relaxed S_1 or S_2 excited state geometry, both of which were computed in the appropriate solvent at the listed level of theory.

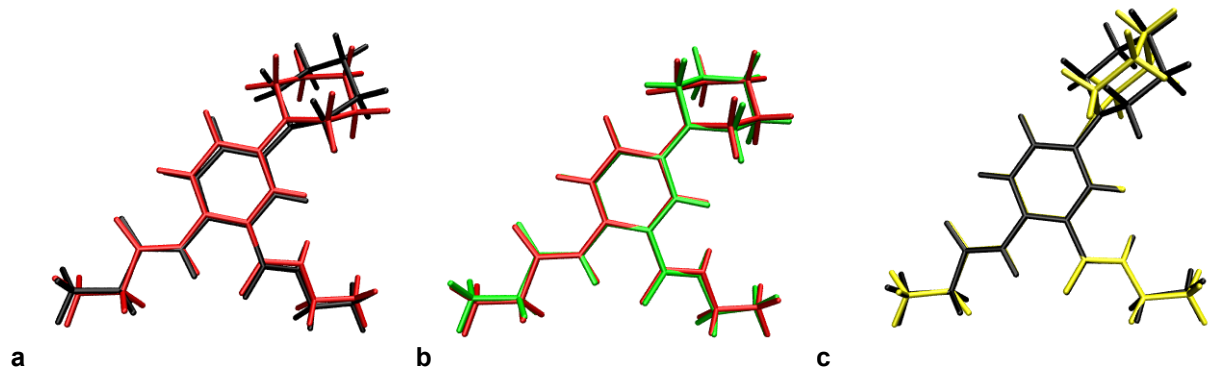

Figure S10. Structure overlays between **(a)** the Aa ground state (black) and relaxed S_1 (red), **(b)** the radical cation (green) and relaxed S_1 (red), and **(c)** the ground state (black) relaxed S_2 (yellow) as calculated with DFT and TDDFT for DCM as a solvent media. Upon relaxation of the S_1 state, the piperidinyl ring shifts to a conformation that is nearly identical to that of the radical. In contrast, the piperidinyl ring in S_2 twists relative to the plane of the molecule. In all cases, the amide bond region of the molecule does not change appreciably. For these calculations, Aa structures with truncated aliphatic chains were used.

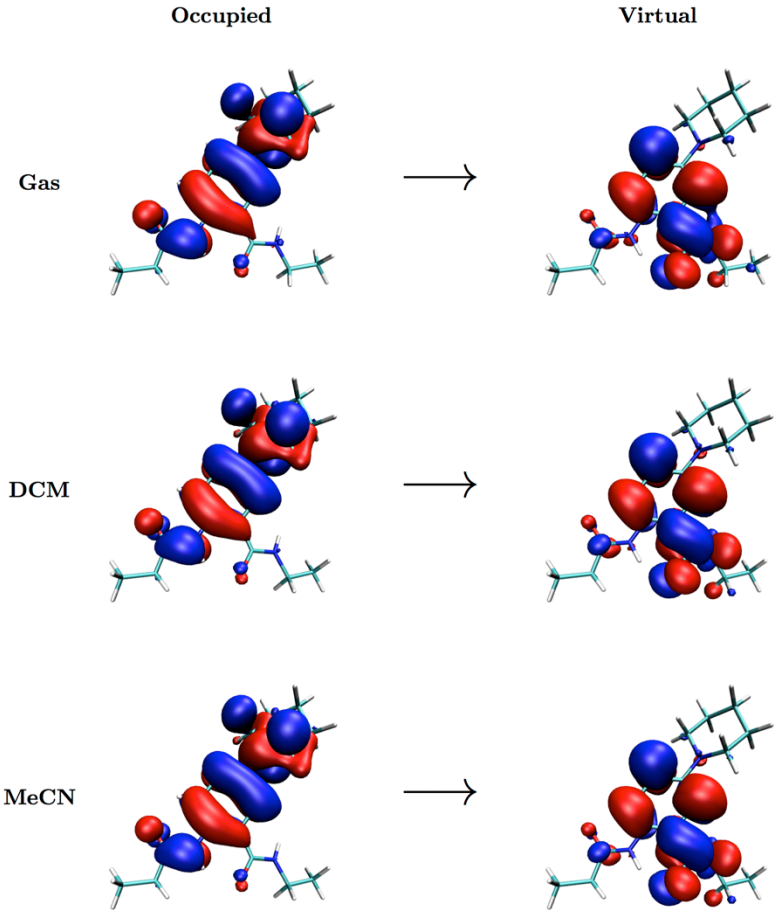

Figure S11. Dominant natural transition orbitals for the $S_0 \rightarrow S_1$ transition in each solvent environment. Changing the solvent has minimal impact on the transition orbitals.

As shown in Table S1, changing the density functional or basis set alters the excitation energies by only ~0.1–0.2 eV. Changing the solvent environment has a similarly small effect. One typically expects errors on the order of a few tenths of a cm^{-1} with TDDFT for valence excited states, so these variations lie well within the experimental error.

Optimized geometries. Given the small differences in the excitation energies, it is not surprising that the optimized geometries do not depend strongly on the solvent model (Figure S8) or the particular density functional and basis set used (Figure S9).

Nature of the excited states. Figure S11 shows the natural transition orbitals for $S_0 \rightarrow S_1$ at the Aa ground state (S_0) geometry in each of the different solvation environments. In all cases, the excitation is dominated by the HOMO → LUMO transition, and it shifts electron density toward the C-terminus amide (right side in the figures). Changing the polarity of the environment does not alter the excitation character. As shown in Table S2, the nature of the excitation is also consistent across basis sets and density functionals. Similar solvent-independence is observed for the $S_0 \rightarrow S_2$ transition (Figure S12), which primarily corresponds to a HOMO → LUMO+1 transition.

Finally, structure relaxation on the S_1 state does not significantly alter the fact that electron density is shifted toward the C-terminus amide in the S_1 state.

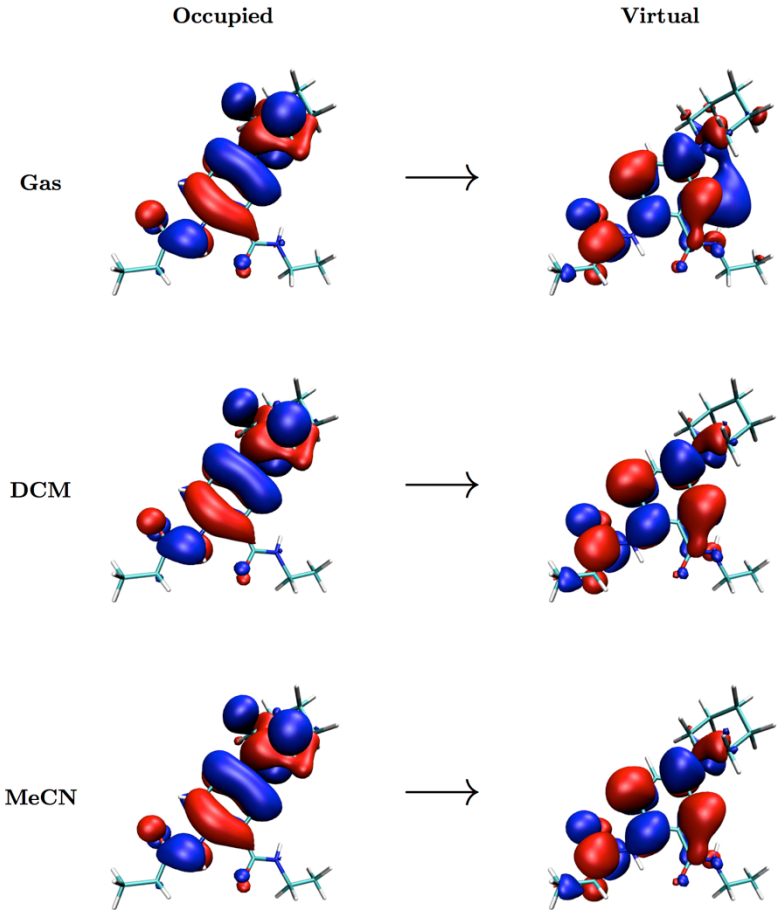

Figure S12. Dominant natural transition orbitals for the $S_0 \rightarrow S_2$ transition in each solvent environment. Changing the solvent has minimal impact on the transition orbitals.

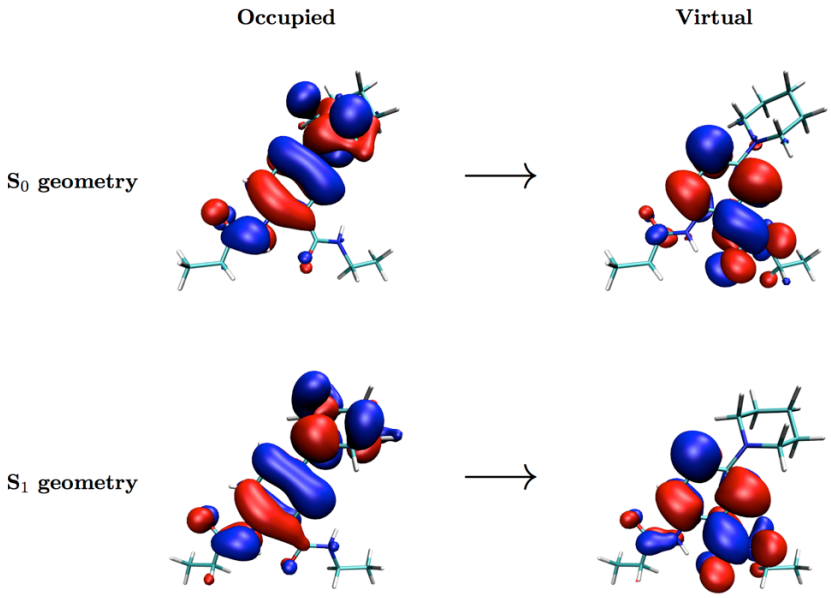

Figure S13. Dominant natural transition orbitals for the $S_0 \rightarrow S_1$ transition at the ground state vs. relaxed S_1 geometry in DCM. Relaxing the structure on the Aa S_1 surface has only a small impact on the transition orbitals.

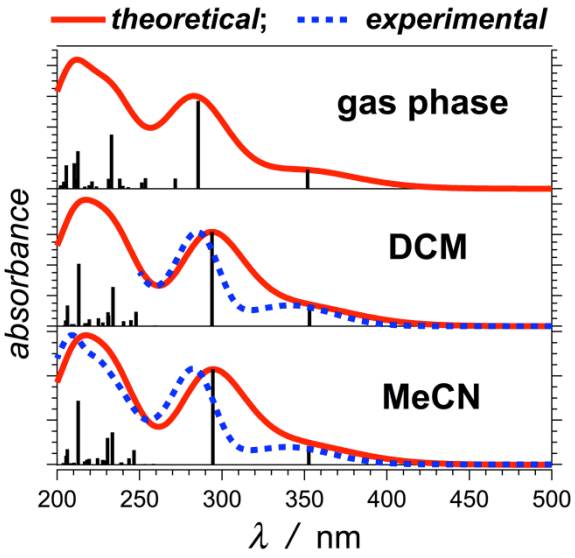

Figure S14. Comparison between experimentally measured and theoretically predicted spectra of Aa for different media; predicted spectra from TDDFT at the B3LYP/6-311+G(d,p). Vertical excitation energies and oscillator strengths are plotted as sticks. The simulated spectra were generated by broadening each peak with a width of 0.333 eV at half maximum. The calculations indicate that the solvation model has a small effect on the Aa excitation spectrum, particularly for the S_1 state near 350 nm, which is confirmed by the experiment results.

References

(1) Zhou, J. S.; Kostic, N. M. *J. Am. Chem. Soc.* **1993**, *115*, 10796-10804.
(2) Davis, W. B.; Ratner, M. A.; Wasielewski, M. R. *J. Am. Chem. Soc.* **2001**, *123*, 7877-7886.
(3) Danyal, K.; Mayweather, D.; Dean, D. R.; Seefeldt, L. C.; Hoffman, B. M. *J. Am. Chem. Soc.* **2010**, *132*, 6894–6895.
(4) Bao, D.; Millare, B.; Xia, W.; Steyer, B. G.; Gerasimenko, A. A.; Ferreira, A.; Contreras, A.; Vullev, V. I. *J. Phys. Chem. A* **2009**, *113*, 1259-1267.
(5) Bao, D.; Ramu, S.; Contreras, A.; Upadhyayula, S.; Vasquez, J. M.; Beran, G.; Vullev, V. I. *J. Phys. Chem. B* **2010**, *114*, 14467-14479.
(6) Upadhyayula, S.; Bao, D.; Millare, B.; Sylvia, S. S.; Habib, K. M. M.; Ashraf, K.; Ferreira, A.; Bishop, S.; Bonderer, R.; Baqai, S.; Jing, X.; Penchev, M.; Ozkan, M.; Ozkan, C. S.; Lake, R. K.; Vullev, V. I. *J. Phys. Chem. B* **2011**, *115*, 9473-9490.

(7) Upadhyayula, S.; Quinata, T.; Bishop, S.; Gupta, S.; Johnson, N. R.; Bahmani, B.; Bozhilov, K.; Stubbs, J.; Jreij, P.; Nallagatla, P.; Vullev, V. I. Coatings of Polyethylene Glycol for Suppressing Adhesion between Solid Microspheres and Flat Surfaces. *Langmuir* **2012**, *28*, 5059-5069.
(8) Wan, J.; Ferreira, A.; Xia, W.; Chow, C. H.; Takechi, K.; Kamat, P. V.; Jones, G.; Vullev, V. I. *J. Photochem. Photobiol., A* **2008**, *197*, 364-374.
(9) Guo, S.; Bao, D.; Upadhyayula, S.; Wang, W.; Guvenc, A. B.; Kyle, J. R.; Hosseinibay, H.; Bozhilov, K. N.; Vullev, V. I.; Ozkan, C. S.; Ozkan, M. *Adv. Funct. Mater.* **2013**, *23*, 5199-5211.
(10) Nuñez, V.; Upadhyayula, S.; Millare, B.; Larsen, J. M.; Hadian, A.; Shin, S.; Vandrangi, P.; Gupta, S.; Xu, H.; Lin, A. P.; Georgiev, G. Y.; Vullev, V. I. *Anal. Chem.* **2013**, *85*, 4567-4577.
(11) Jones, G., II; Zhou, X.; Vullev, V. I. *Photochem. Photobiol. Sci.* **2003**, *2*, 1080-1087.
(12) Fox, M. A.; Galoppini, E. *J. Am. Chem. Soc.* **1997**, *119*, 5277-5285.
(13) Galoppini, E.; Fox, M. A. *J. Am. Chem. Soc.* **1996**, *118*, 2299-2300.
(14) Jortner, J. *J. Chem. Phys.* **1976**, *64*, 4860-4867.
(15) Tanaka, S.; Marcus, R. A. *J. Phys. Chem. B* **1997**, *101*, 5031-5045.
(16) Barbara, P. F.; Meyer, T. J.; Ratner, M. A. *J. Phys. Chem.* **1996**, *100*, 13148-13168.
(17) Marcus, R. A. *J. Electroanal. Chem.* **2000**, *483*, 2-6.
(18) Becke, A. D. *J. Chem. Phys.* **1993**, *98*, 5648-5652.
(19) Lee, C. T.; Yang, W. T.; Parr, R. G. *Phys. Rev. B* **1988**, *37*, 785-789.
(20) Krishnan, R.; Binkley, J. S.; Seeger, R.; Pople, J. A. *J. Chem. Phys.* **1980**, *72*, 650-654.
(21) Frisch, M. J. *et al.*, Gaussian 09 Revision A.1, Gaussian Inc. Wallingford CT, 2009.
(22) Tomasi, J.; Mennucci, B.; Cammi, R. *Chem. Rev.* **2005**, *105*, 2999-3093.
(23) Martin, R. L. *J. Chem. Phys.* **2003**, *118*, 4775-4777.
(24) Hehre, W. J.; Ditchfie.R; Pople, J. A. *J. Chem. Phys.* **1972**, *56*, 2257-2261.
(25) Harihara, P. C.; Pople, J. A. *Theoret. Chim. Acta* **1973**, *28*, 213-222.
(26) Adamo, C.; Barone, V. *J. Chem. Phys.* **1999**, *110*, 6158-6170.